



This is a repository copy of *High-speed imaging of light-induced photoreceptor microsaccades in compound eyes*.

White Rose Research Online URL for this paper:
<https://eprints.whiterose.ac.uk/182846/>

Version: Submitted Version

Article:

Kemppainen, J. orcid.org/0000-0002-9140-6932, Mansour, N., Takalo, J. orcid.org/0000-0002-1638-0808 et al. (1 more author) (Submitted: 2021) High-speed imaging of light-induced photoreceptor microsaccades in compound eyes. bioRxiv. (Submitted)

<https://doi.org/10.1101/2021.07.22.453335>

Reuse

This article is distributed under the terms of the Creative Commons Attribution-NonCommercial-NoDerivs (CC BY-NC-ND) licence. This licence only allows you to download this work and share it with others as long as you credit the authors, but you can't change the article in any way or use it commercially. More information and the full terms of the licence here: <https://creativecommons.org/licenses/>

Takedown

If you consider content in White Rose Research Online to be in breach of UK law, please notify us by emailing eprints@whiterose.ac.uk including the URL of the record and the reason for the withdrawal request.



eprints@whiterose.ac.uk
<https://eprints.whiterose.ac.uk/>

High-speed imaging of light-induced photoreceptor microsaccades in compound eyes

Joni Kemppainen¹, Neveen Mansour¹, Jouni Takalo¹ & Mikko Juusola^{1,2*}

¹Department of Biomedical Science, University of Sheffield, Sheffield S10 2TN, UK

²National Key Laboratory of Cognitive Neuroscience and Learning, Beijing, Beijing Normal University, Beijing 100875, China.

* **Correspondence:** Mikko Juusola

m.juusola@sheffield.ac.uk

Keywords: photoreceptor, open rhabdom, fused rhabdom, microsaccade, *Drosophila*, deep pseudopupil, goniometry, hyperacuity, active sampling, active vision

Abstract

Inside compound eyes, photoreceptors contract to light changes, sharpening retinal images of the moving world in time. Current methods to measure these so-called photoreceptor microsaccades in living insects are spatially limited and technically challenging. Here, we present goniometric high-speed deep pseudopupil (GHS-DPP) microscopy to assess how the rhabdomeric insect photoreceptors and their microsaccades are organised across the compound eyes. This method enables non-invasive rhabdomere orientation mapping, whilst their microsaccades can be locally light-activated, revealing the eyes' underlying active sampling motifs. By comparing the microsaccades in wild-type *Drosophila*'s open rhabdom eyes to *spam*-mutant eyes, reverted to an ancestral fused rhabdom state, and honeybee's fused rhabdom eyes, we show how different eye types sample light

26 information. These results show different ways compound eyes initiate the conversion of spatial light
27 patterns in the environment into temporal neural signals and highlight how this active sampling can
28 evolve with insects' visual needs.

29

30 **Introduction**

31 Because the insect compound eyes extend from the rigid head exoskeleton, appearing stationary to
32 an outside observer, it was long assumed that their inner workings would also be static. Therefore, as
33 the eyes' ommatidial faceting sets their photoreceptor spacing, it was deduced that the compound
34 eyes could only sample a pixelated low-resolution image of the world¹⁻³.

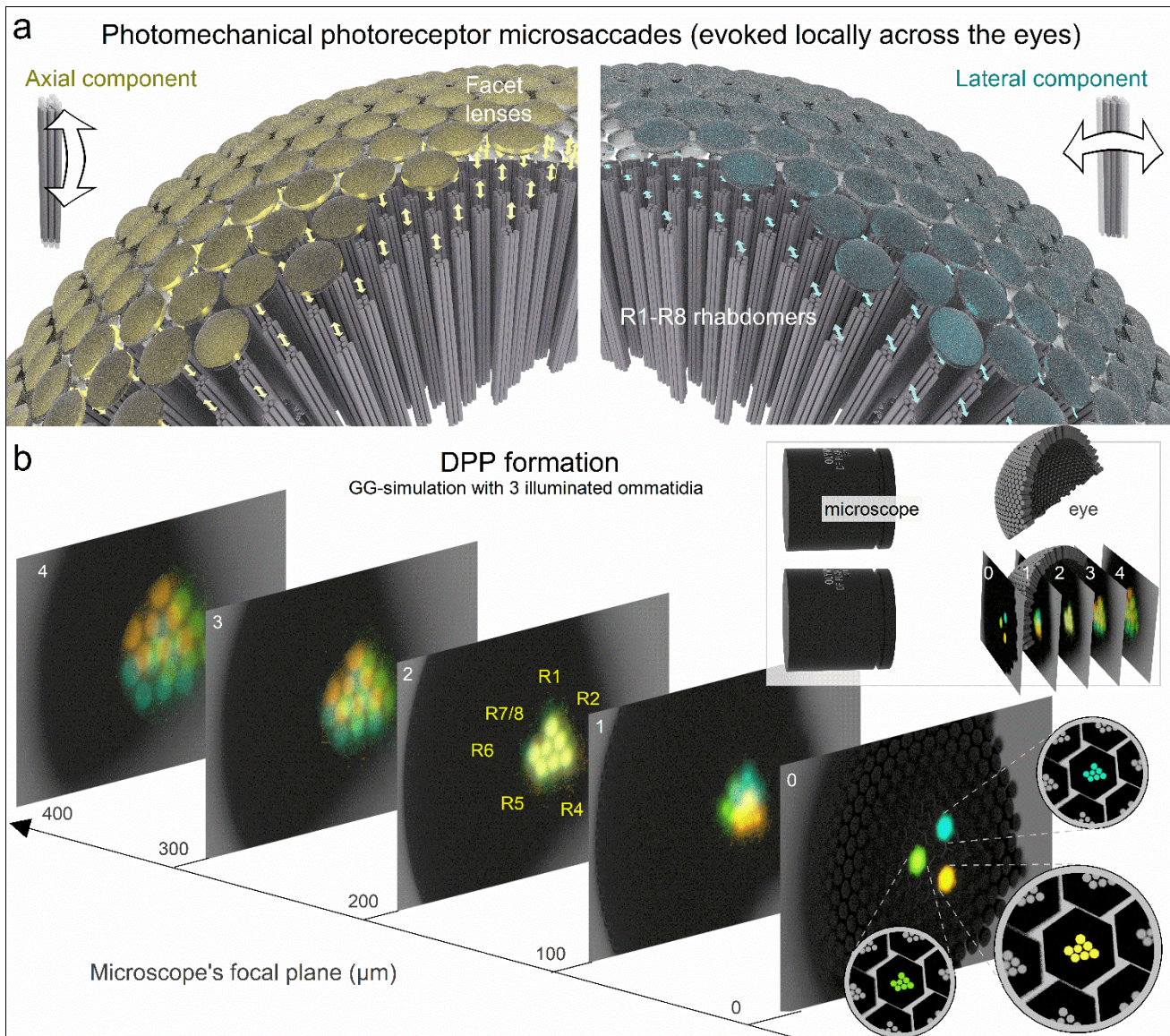


Fig. 1 | Active sampling by photomechanical photoreceptor microsaccades and the deep pseudopupil phenomena. **a**, In the conventional static sampling theory^{1,2}, ommatidial facets set a compound eye's photoreceptor spacing, limiting the finest image details the eye could resolve. However, inside an ommatidium, incoming light intensity changes make its R1-R7/8 photoreceptors rapidly recoil axially and swing laterally. These so-called ultrafast photoreceptor microsaccades enable *Drosophila* to see the world in a finer resolution than its eyes' photoreceptor spacing, explained by the new active sampling theory^{4,5}. Left: *Drosophila* eye computer graphics (CG) model highlights the axial microsaccade component; R1-R7/8s first recoil and then slide towards the ommatidium lens. Right: concurrently, the light-activated R1-R7/8 also swing sideways (laterally).

A local (incident) light intensity change evokes microsaccades only in those ommatidia facing the stimulus. If this happens in the frontal left and right eye ommatidia with overlapping receptive fields, their microsaccades are synchronous yet have mirror-symmetric lateral components^{4, 5}. Meanwhile, elsewhere across the eyes, the photoreceptors stay still because the eye curvature and the ommatidial screening pigments block them from seeing the stimulus^{4, 5}. **b**, The optical principle of the deep pseudopupil (DPP). DPP is a virtual image of several distal R1-R7/8 rhabdomere tips (highlighted in blue, yellow and green for three nearby ommatidia), which align with the angle the eye is observed at while being ~10x-magnified by the ommatidial lens system. These virtual rhabdomere images are optically brought together when the microscopes' focal plane is ~200 µm under the eye surface (as shown in image 2). Because of the optical magnification, the rhabdomere tips, which appear deep inside the eye, are actually positioned at ~20 µm from the inner surface of the ommatidium lens.

35

36 However, recent results on the *Drosophila* compound eyes are now replacing this *static* viewpoint with
37 a new concept of morphodynamic *active* sampling^{4, 5}. Sophisticated experiments have revealed how
38 photoreceptor microsaccades *locally*^{4, 5} (**Fig. 1a**) and intraocular muscle contractions *globally*⁴⁻⁷ move,
39 stretch and recoil intraommatidial optical structures, improving vision morphodynamically. During the
40 *local ultrafast* (<100 ms) *photomechanical* microsaccades, the photoreceptors of a single ommatidium
41 concurrently recoil axially (**Fig. 1a**, left) and swing laterally (right) to increase sampling resolution in
42 space and sharpen light input in time for super-resolution vision⁴. And, with the left and right eye
43 photoreceptor pairs generating mirror-symmetric microsaccades, this active sampling further expands
44 the flies' hyperacute stereopsis⁵. Conversely, the intraocular muscle contractions shift one eye's entire
45 retina (its sampling matrix) *globally* regarding the other eye⁴⁻⁷. In head-immobilised *Drosophila*, these
46 drifts and vergence movements, which also happen underneath the eyes' rigid ommatidial lens cover,
47 hidden from the outside view, are typically 10-to-100-times slower than the local photoreceptor
48 microsaccades^{4, 5}. But in freely behaving flies⁶, their dynamics may strengthen to combat adaptive
49 perceptual fading^{4, 7} and contribute to attentive saccadic viewing and object tracking⁶.

50

51 Minute photomechanical photoreceptor contractions ($< \sim 200$ nm) were first measured in *ex vivo*
52 *Drosophila* preparations using atomic force microscopy (AFM)⁸. Initially, these movements, caused
53 by PIP₂ cleavage in the microvillar photoreceptor membrane^{8,9}, were thought to be too small to alter
54 the photoreceptors' light input⁸. However, later live-microscopy experiments⁴, using the cornea
55 neutralisation method¹⁰, showed that *ex vivo* AFM underestimates the size of the lateral rhabdomere
56 movements⁴. Intense light modulation *in vivo* could rapidly swing an R1-R6 rhabdomere about its
57 width ($\sim 1,400$ nm) sideways. And with similar microsaccades also occurring in synaptically decoupled
58 photoreceptors⁴, the results demonstrated active sampling inside an ommatidium for the first time⁴.
59 Unfortunately, both these methods are technically demanding and spatially limiting and thus ill-suited
60 for mapping the microsaccade movement sizes and directions across the left and right compound
61 eyes.

62

63 In the *Drosophila* compound eyes, an optical phenomenon called the deep pseudopupil (DPP) arises
64 from the regular arrangement of ommatidia (**Fig. 1b**), each containing R1-R7/8 photoreceptors in
65 which open rhabdomeres act as waveguides¹¹. By focussing a microscope's image plane below the
66 eye's outer surface (**Fig. 1b**, inset), virtual images of several ommatidia's R1-R7/8 rhabdomere
67 patterns (**Fig. 1b**, highlighted in blue, green and yellow for the nearby ommatidia) become
68 superimposed, revealing their stereotypical yet ~ 10 -times magnified trapezoid arrangement. And
69 since these virtual images fuse at the microscope focal plane of ~ 200 μm , we see the rhabdomere
70 tips inside the eye, ~ 20 μm away from the inner surface of their ommatidium lenses. Thus, DPP
71 microscopy offers a versatile, non-invasive method to observe retinal tissue in living flies and other
72 insects (**Fig. 2**). First, to observe a well-defined, clear DPP pattern in dipteran eyes requires precisely
73 organised rhabdomeres across the neighbouring ommatidia¹², and DPP microscopy with epi-
74 illumination^{13, 14} (frontally, through the eye optics) has been used to study retinal degeneration that
75 breaks this order¹⁵⁻¹⁷. Second, because the rhabdomeres contributing to the DPP image are those
76 facing the observer, the DPP microscopy provides the "gold standard" measure for the binocular

77 overlap over the left and right compound eyes¹⁸⁻²⁰. Finally, because any lateral retinal tissue
78 movement shifts the DPP similarly, DPP microscopy can be used to investigate how the eye-muscle-
79 induced retinal micromovements shift the photoreceptors' receptive fields^{5, 21}.
80

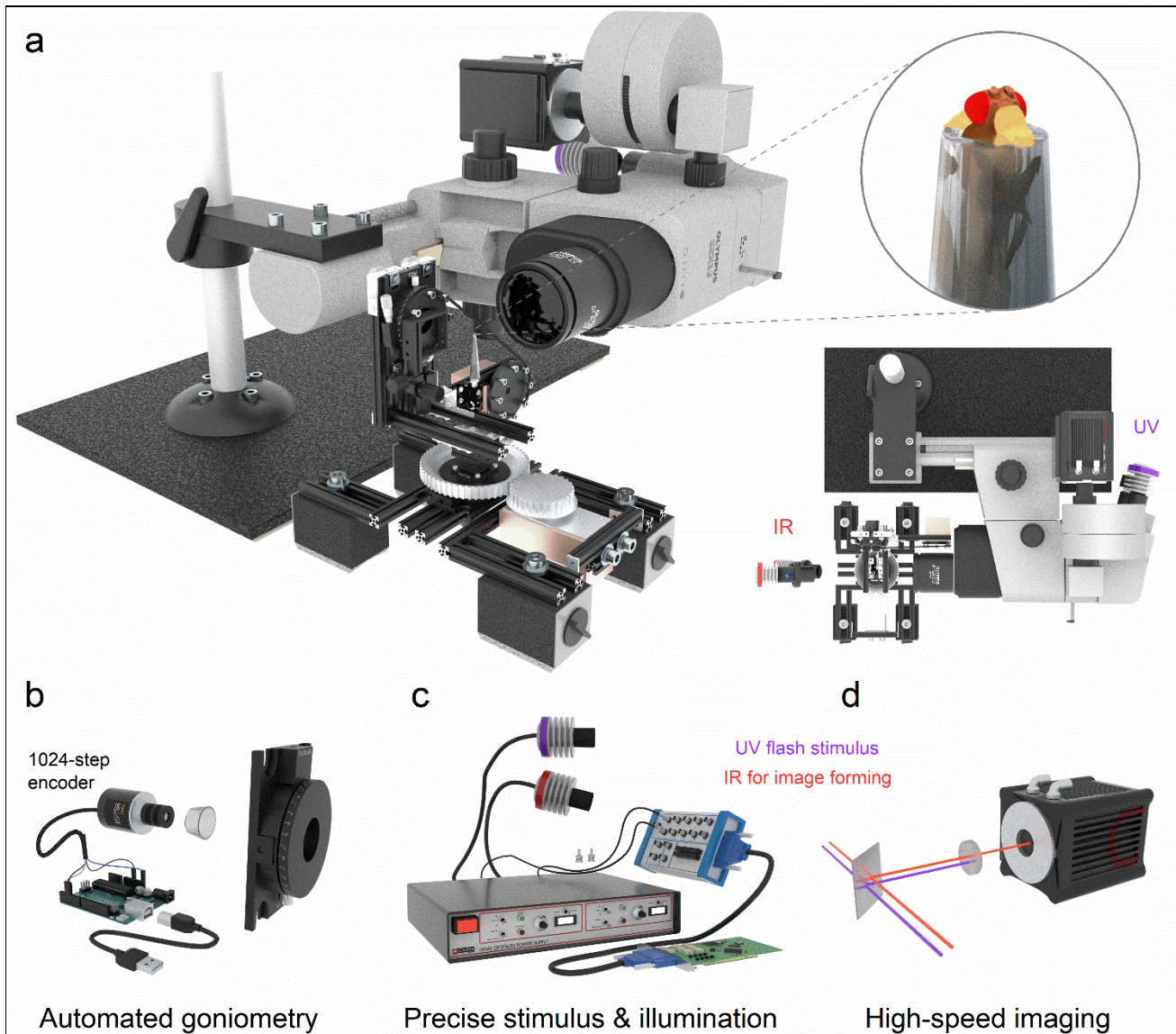


Fig. 2 | Goniometric high-speed deep pseudopupil (GHS-DPP) imaging system. a, Its integral parts are a sideways mounted stereo microscope with a high-speed (100-1,000 fps) digital camera and a goniometric rotation stage system. *Drosophila* eyes are imaged under the antidromic dual infrared illumination, invisible to the flies^{4, 22}. Photoreceptor microsaccades are activated by ultraviolet (UV or green) light stimulation, delivered through the ocular slot system. **b**, The fly's x/y-

rotations are read using a 1,024-step rotary encoder and an Arduino board. **c**, The high-power LEDs and the camera were controlled over the BNC interface. **d**, An infrared (IR) passing but UV blocking optical filter in the front of the camera decouples the UV-stimulus from the imaging pathway. See **Supplementary Video 1**.

81

82 Here, we present a novel goniometric high-speed deep pseudopupil (GHS-DPP) microscopy (**Fig. 2**)
83 with invisible (850 nm) infrared back-illumination, developed to study active sampling in insect
84 compound eyes. We first use it to measure the photoreceptor microsaccade dynamics and directions
85 in wild-type *Drosophila melanogaster*, possessing the archetypical open rhabdom dipteran eyes (**Fig.**
86 **3**, top), and transgenic *spam* null-mutants, in which rhabdomeres fail to separate (**Fig. 3**, middle),
87 forming an ancestral, fused rhabdom (apposition) eye²³. Finally, we measure photoreceptor
88 microsaccades in the Honeybee (*Apis mellifera*) apposition eyes (Fig. 3, bottom) and compare these
89 dynamics to wild-type and *spam Drosophila*. Our results show that active sampling by photoreceptor
90 microsaccades occurs both in the open and fused rhabdom eyes. We analyse their functional
91 similarities and differences and discuss what these results could mean for the evolution of compound
92 eyes and insect vision in general²⁴.

93

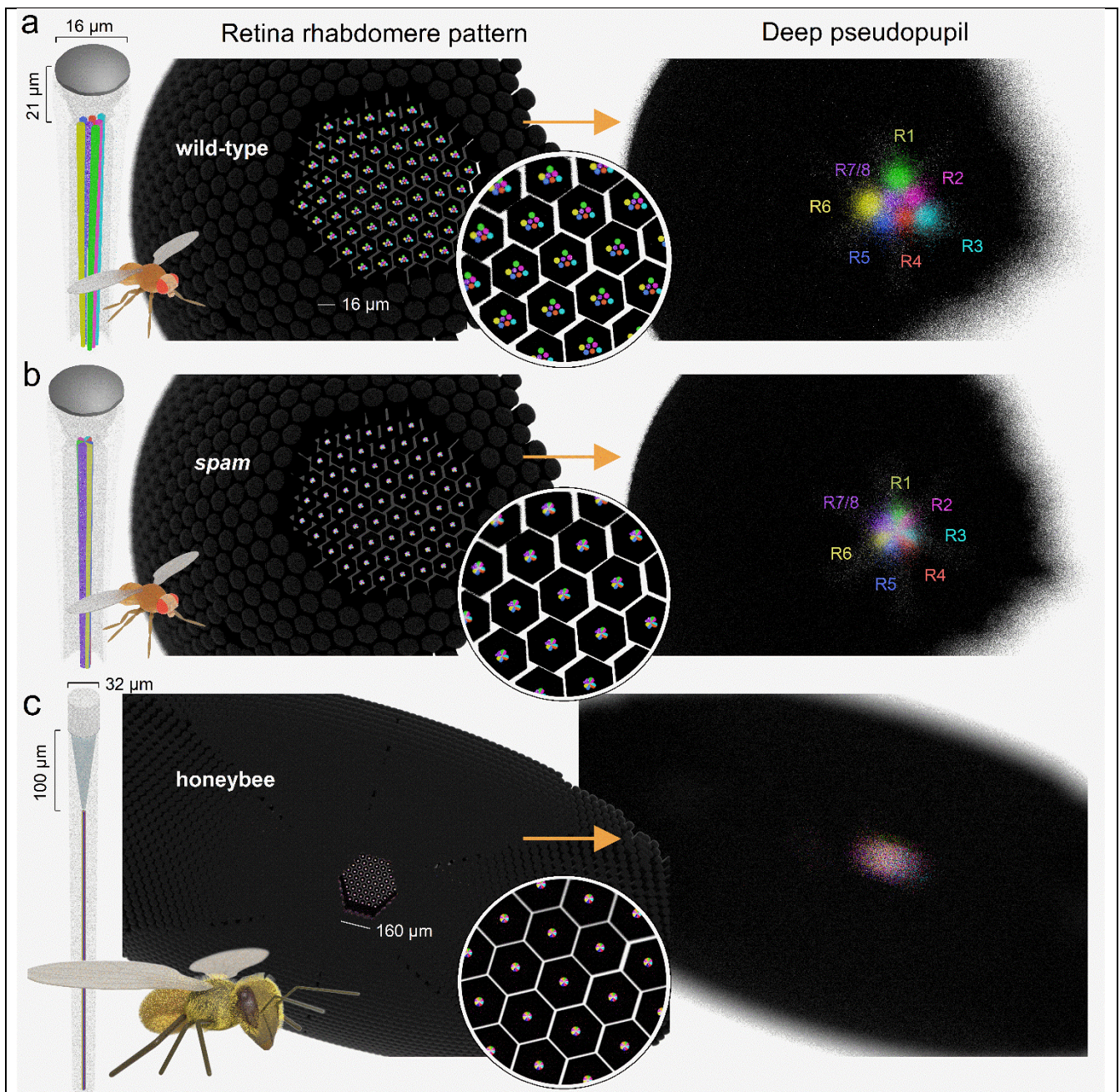


Fig. 3 | Deep pseudopupil (DPP) in the wild-type and *spam* *Drosophila* and honeybee apposition eyes. a, Left: the *Drosophila* compound eye comprises ~750 ommatidia, each having a light focusing facet lens and eight photoreceptors; with their light-sensitive parts, the rhabdomeres (coloured), protruding centrally. Middle: Computer graphics (CG) models of the open wild-type rhabdomeres; here shown for their left eye's southern hemisphere. Right: The CG-model simulated DPP image appears as a magnified "virtual" image of the open rhabdomere patterns. Here, DPP is

shown at the focal plane of 200 μm into the eye for the right eye ventral section, corresponding to frame #2 in **Fig. 1b** and the bottom-left frame in **Fig 4b**.

b, Left: in the *spam*, R1-R7/8 rhabdomeres reverted back into their ancestral fused rhabdom form. Middle: inside the ommatidia (in the retinal tissue), the fused rhabdom resembles a single rod. Right: their DPP appears as a tiny bright disc. Colouring indicates the contributing R1-R7/8 rhabdomeres' relative locations in the virtual DPP rhabdom image.

c, Left and Middle: In the honeybee apposition eye ommatidia, the photoreceptor rhabdomeres form a single rod-like waveguide, the rhabdom, centred $\sim 100 \mu\text{m}$ behind the ommatidial lens.

Right: In the DPP image, the honeybee fused rhabdom appears as a single disk, similar to *spam*.

94

95 **Results**

96 **Left and right eye DPP patterning rotate systematically and mirror-symmetrically**

97 We first inspected the wild-type and *spam* flies' DPP patterns in still images taken under antidromic
98 infrared illumination in perceptual darkness (**Fig. 4**). Characteristically, the wild-type DPP image
99 merged the neighbouring ommatidia's R1-R7/8 rhabdomere images into a classic trapezoid pattern of
100 seven small bright discs (**Fig. 4a**). In contrast, the *spam* DPP appeared as a tiny bright disc (**Fig. 4d**).
101 These different DPP patterns were entirely expected, as they directly follow the deep pseudopupil
102 theory¹² (**Fig. 1b**) and are reproduced by our CG-modelling (**Fig. 3**).

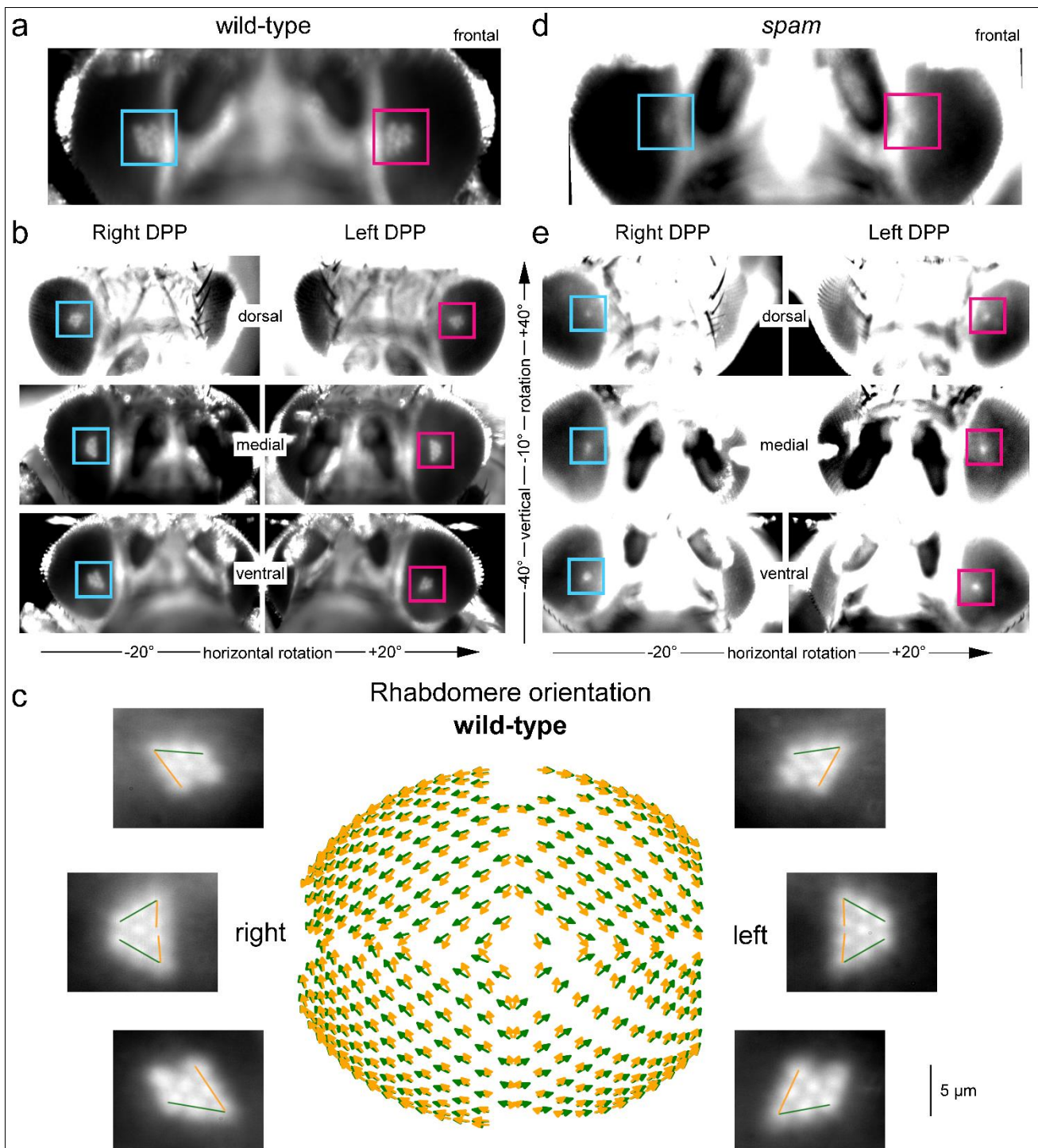


Fig. 4 | Wild-type and *spam* DPP imaged by the 850 nm GHS-DPP microscopy. a, Forward-facing wild-type eyes (horizontal rotation = 0°) with the red and blue square boxes indicating their left and right DPPs, respectively. **b,** Wild-type eyes, viewed on the dorsal side (1st row), at the midline (2nd row), and on the ventral side (3rd row), reveal their DPPS ventral-dorsal symmetry. **c,** The wild-type rhabdomere orientation across the left and right eyes as mapped with the GHS-DPP

microscopy. The green lines indicate the R1-R2-R3 rhabdomere axes, and the yellow lines the R3-R4-R5 axes. R1-R7/8 rhabdomeres rotate systematically with changing eye location, producing concentrically-expanding diamonds-patterns⁵, highlighting the characteristic right-left eye and north-south (dorsal-ventral) hemisphere mirror-symmetry. **d**, The left and right eye *spam* DPPs appear circular-symmetric discs and are more oversaturated due to their eyes' lighter pigmentation. **(e)** *spam* eyes with their DPPs are viewed on the dorsal side, midline, and ventral side.

103

104 Because *Drosophila* has a small head and fairly transparent (not densely pigmented) cuticle, the
105 infrared GHS-DPP microscopy makes it straightforward to record, measure and map the DPP pattern
106 changes across the eyes. Specifically, for *Drosophila*, we could use relatively low-power infrared
107 illumination - propagating through its intact head - and still obtain high signal-to-noise DPP imaging at
108 high frame rates (≥ 100 fps). The real benefit was that since the tested flies required no surgical cuticle
109 removal (to improve infrared throughput for better DPP image quality) and suffered very little or no
110 heat damage, individual *Drosophila* regularly provided consistent, repeatable results throughout
111 hours-long experiments.

112

113 In the wild-type, the left and right eyes' DPPs are mirror-symmetric: shown in the binocular upper-
114 frontal view (**Fig. 4a**; the blue and red boxes highlight their right and left DPPs, respectively).
115 Interestingly, the north and south hemispheres of the eye also have mirror-symmetric DPP patterns²⁵
116 but fuse at the equator (mid-line) to form larger elongated triangle shapes (**Fig. 4b**). The DPP
117 orientation, as the angular rotation between R3-R2-R1 rhabdomeres (yellow line) and R3-R4-R5
118 rhabdomeres (green), shifts between nearby eye locations in regular small steps, generating the left
119 and right eyes' mirror-symmetric global map (**Fig. 4c**). In this global map, local DPP alignments follow
120 a concentrically expanding diamond-shaped pattern. Therefore, the underlying developmentally
121 rotated R1-R7/8 rhabdomere orientations at each eye position align with the frontally expanding optic
122 flow field⁵ (**Supplementary Video 3**). On the contrary, in the *spam* mutant, because their DPPs

123 appear as homogeneous circular or oval discs (**Fig. 4d**), neither such gradual rotations nor their left-
124 right and north-south divisions were readily observable (**Fig. 4e**).

125

126 **Photoreceptor microsaccades' lateral and axial components**

127 After imaging the eyes' DPPs, we tested whether the *spam* eyes can generate ultrafast (time-to-peak
128 <100 ms) photomechanical microsaccades, akin to the open rhabdom wild-type^{4, 5} eyes. In the first
129 instance (**Fig. 5a and b**), these experiments were performed at the fixed left and right eye locations
130 ($\pm 28^\circ$ horizontal, -37° vertical) using a bright 200-ms-long ultraviolet (365 nm) flash stimulus
131 (**Supplementary Video 2**). In each fly, the UV flash was delivered locally at the centre of the observed
132 DPP photoreceptors' receptive fields (**Supplementary Video 4**) and repeated 25 times to obtain
133 robust estimates and statistics of the resulting response dynamics.

134

135 A flash of any wavelength R1-R8 photoreceptors are sensitive to (~ 300 to ~ 650 nm)^{22, 26} evokes a
136 photoreceptor microsaccade⁵. Inside an ommatidium, the number of light-activated photoreceptors
137 and their combined contraction strength set its photoreceptor microsaccade amplitude⁵. Because
138 these photoreceptors are mechanically coupled and likely pivoted⁵, it only takes one (say R1) to be
139 light-activated, and its contraction alone can move its neighbours (R2-R8) too⁵ (**Supplementary**
140 **Video 4**). As *Drosophila* R1-R6 possesses the sensitising UV-pigment and R7s are UV-sensitive^{22, 26},
141 a UV-flash evokes larger photoreceptor microsaccades than, say, an amber-flash, which only
142 activates R8y cells⁵. Therefore, in *Drosophila* experiments, UV-flash is a good choice of stimulus.

143

144 In wild-type, a UV flash always evoked a local photomechanical photoreceptor microsaccade, making
145 the observed DPP rapidly jump laterally in the front-to-back (north-west) direction (**Fig. 5c**) before
146 swiftly returning in darkness, as expected for normal eye function^{4, 5}. However, remarkably, we found
147 that the fused rhabdom *spam* eyes also generate robust ultrafast DPP microsaccades (**Fig. 5d**) with
148 broadly similar temporal dynamics. In both phenotypes, besides moving laterally (**Fig. 5d**, above), the
149 photoreceptors moved simultaneously also axially (below). This axial component, resulting from the

150 rhabdomeres contracting away and elongating towards the ommatidium lens (and the camera)⁵, can
151 be directly measured as a proportional DPP darkening and lightening⁵. To eliminate any motion
152 artefacts, we measured the axial component from the DPP image pixels' dynamic intensity change,
153 tracking frame-by-frame only the pixels within the rhabdomere tips. As expected, the fast axial DPP
154 brightness changes systematically time-locked with the corresponding lateral DPP movements (**Fig.**
155 **5d-f**), consistent with both phenotypes having the same photomechanical phototransduction origin.

156
157 Qualitatively, both the wild-type and *spam* had similar looking microsaccade kinematics and
158 probabilities (**Fig. 5d-f**), but the overall displacement amplitudes appeared much smaller in *spam* (**Fig.**
159 **5d**, below). Maximum amplitude measurements confirmed that the *spam* DPP microsaccades (both
160 their lateral and axial components) were indeed smaller than the wild-type (**Fig. 5g**). Similarly, the
161 *spam* flies' calculated maximum microsaccade activation speed was significantly slower (**Fig. 5h**).
162 However, these phenotypes' logarithmic growth factors during the activation phase did not differ
163 statistically (**Fig. 5i**), meaning that the *spam* DPP microsaccades' slower speed resulted from their
164 shorter travelling distance but not from changes in their duration. Accordingly, there was no significant
165 change in the half-rise times (**Fig. 5j**). The similar logarithmic growth factors and half-rise times
166 suggest that the likely photomechanical cause of the DPP microsaccades, the PIP₂ cleavage from the
167 microvillar membrane during phototransduction⁸, is unaffected by the *spam* mutation. Overall, these
168 results show that the *spam* flies have similar microsaccade kinematics as the wild-type but are only
169 smaller.

170
171 We further inspected individual flies' DPP microsaccade variations to the 25 times repeated light
172 flashes. A qualitative comparison between the selected wild-type and *spam* flies showed that most
173 variation occurs in the total microsaccade size; that is, how far the DPP and the rhabdomeres travel
174 during the activation phase (**Fig. 5k**). Furthermore, we found no difference between their DPP
175 displacements' standard deviations (**Fig. 5l**), indicating similar intrinsic amplitude jitter, or
176 photomechanical stochasticity, affecting wild-type and *spam* microsaccades. These results highlight

177 that DPP microsaccades vary considerably between the flies and between individual flies' repeated
178 responses, suggesting that their kinematics may further reflect top-down regulation from the brain²⁷.
179 ²⁸, i.e. the flies internal state (circadian rhythm, attention or activity state)^{27, 29, 30}. Such variability could
180 result, for instance, from the slow eye-muscle-induced whole retina drifting⁵, structurally fluctuating
181 the local rhabdomere tension (their anchoring and pivoting dynamics) from one trial to another⁵.
182 Notably, however, the real benefit of the local photoreceptor microsaccades' stochastic variability,
183 irrespective of its cause, is that it effectively removes aliasing from the retinal sampling matrix^{4, 5, 31}.

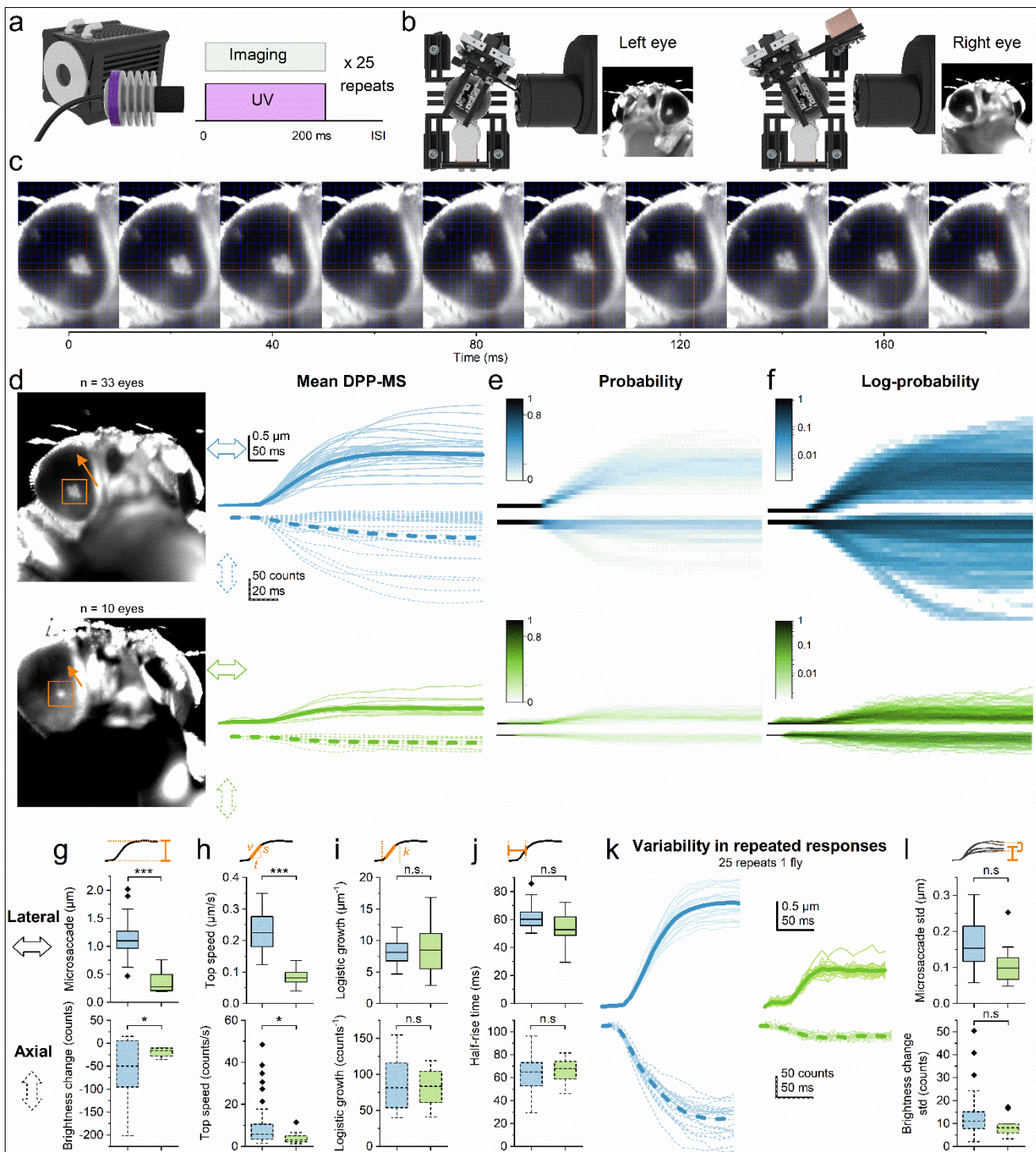


Fig. 5 | DPP microsaccade kinematics in the wild-type and *spam*. **a**, In the local recordings, the UV flash was repeated 25 times following a regular inter-stimulus interval (ISI). **b**, These experiments were done at one fixed location in each eye. **c**, Image time series from the stimulus onset (time zero) to 180 ms later, showing how the same DPP pattern, plotted against fixed red x-y-coordinate axes, moves back-to-front (North-West) about one rhabdomere width (~ 1.5 mm inside

ommatidia). **d**, Wild-type and *spam* DPP patents and their tracked movement directions (orange arrows). Mean rhabdomere lateral (continuous traces) and axial (fast DPP darkening/brightening, dotted) displacement components in the wild-type (1st row) and *spam* (2nd row) appear similar in shape but are smaller in *spam*. The thick lines show the corresponding population means. **e-f**, The probability plots, containing the separate (single) responses, indicate that the photoreceptor microsaccades occur over a predictable but variable range. **g-j**, The microsaccade amplitude, the top speed, the logistic growth factor and the half-rise time, respectively, in the wild-type and *spam* (Welch's t-test; $p = 0.027$, $p = 0.031$, $p = 0.86$, $p = 0.62$). **k**, The DPP microsaccade responses of one selected wild-type and one *spam* show variability in repeated responses that may indicate purposeful modulation. **l**, Quantified displacement standard deviations (std) for all the wild-type and *spam* flies do not differ statistically (Welch's t-test; $p = 0.16$).

184

185 **Mapping photoreceptor microsaccades' movement directions across the eyes**

186 Next, we mapped DPP microsaccades and their directions from about 200 distinct locations over the
187 left and right eyes (**Fig. 6a and b; Supplementary Video 5**). In the wild-type, the DPP microsaccades
188 moved approximately from back-to-front or south-to-north, depending on the eye region (**Fig. 6c**). But
189 we did not image the DPP microsaccade relaxation phase, which occurs during light decrements
190 (darkening), moving slower and in opposite directions to the activation phase^{4, 5} (returning
191 rhabdomeres to their initial starting positions).

192

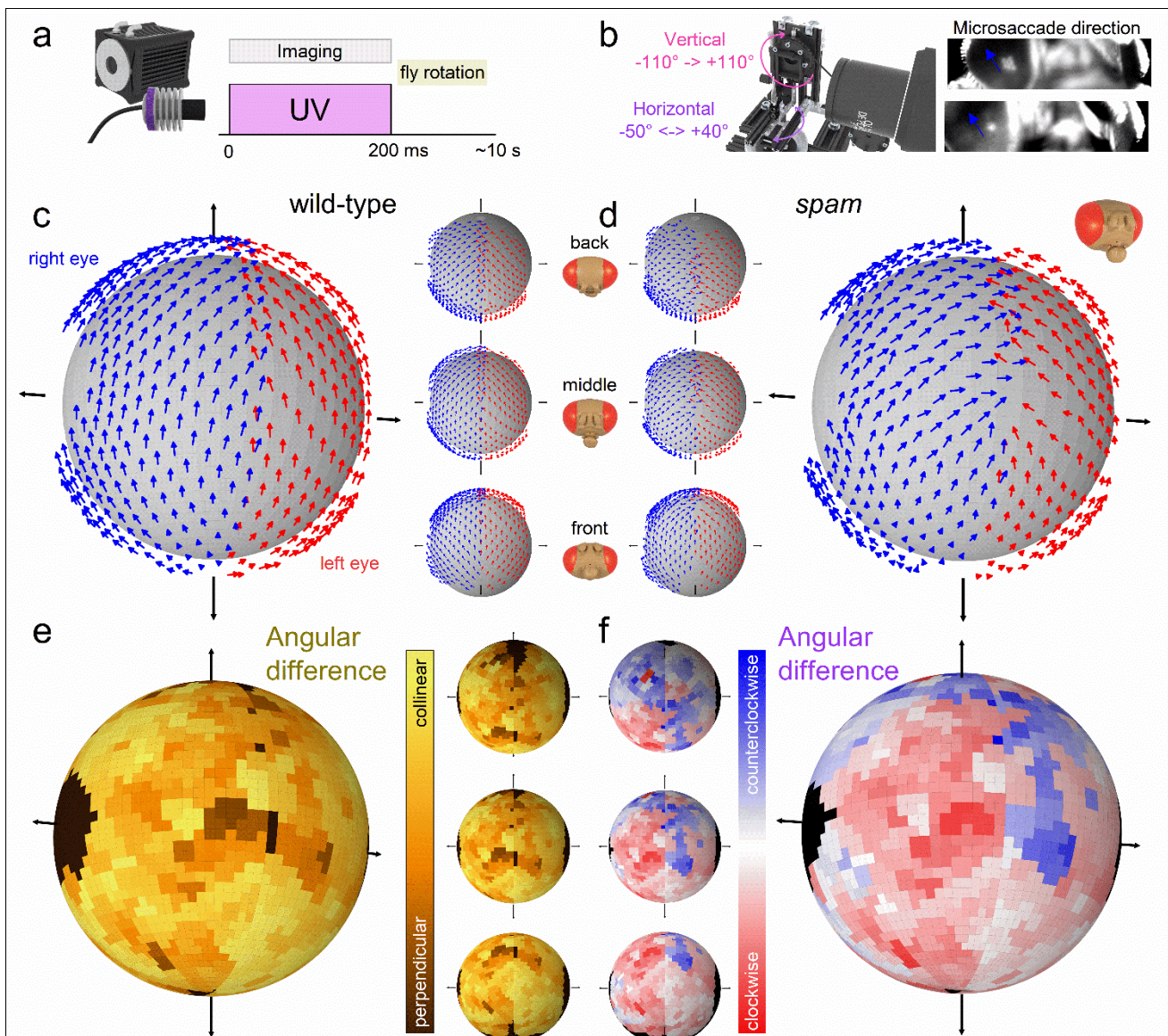


Fig. 6 | DPP microsaccades across the left and right wild-type and *spam* eyes. **a**, During the 200 ms UV flash, the camera recorded the DPP microsaccades 100 frames-per-second. **b**, After each flash, the fly was rotated, recording approximately 200 locations on the left and right eyes. Blue arrows indicate DPP microsaccade directions. **c**, Mean microsaccade vector map of wild-type flies (N = 5; the arrows indicate eye-location-specific normalised microsaccade directions). The small insets show the dorsal, the anterior and the ventral vector map views from the top to bottom. **d**, Mean microsaccade vector map of *spam* files (N=5) appears similar to the wild-type but only slightly noisier. **e**, Angular difference plot of the wild-type and *spam* vector maps show that the wild-type and *spam* vector maps are mostly collinear. **f**, On the anterior eye regions, the angular

difference graph suggests that the *spam* right eye microsaccades are clockwise-rotated and the left eye microsaccades counterclockwise-rotated compared to the wild-type (as viewed from outside). See **Supplementary Videos 2 and 5**.

193

194 Interestingly, we discovered that the fused rhabdom *spam* DPP microsaccades generally moved along
195 similar directions to those of wild-type (**Fig. 6d**). We calculated the absolute angular difference in the
196 rotation of the microsaccades between the wild-type and *spam* flies and found their resulting global
197 maps broadly similar (**Fig. 6e; Supplementary Video 5**). However, in a more detailed inspection, the
198 *spam* left eye DPP microsaccades on the anterior parts showed slightly more counterclockwise
199 rotation and the right eye DPP microsaccades slightly more clockwise rotation than the wild-type (**Fig.**
200 **6f**).

201

202 These results demonstrate active sampling - by photomechanical photoreceptor microsaccades -
203 occurring in a spatially-coordinated manner across the *spam* fused rhabdom eyes. Moreover, since
204 the wild-type microsaccade directions (their forward-and-back movement axes) align with their R1-
205 R2-R3 rhabdomere axis (**Fig. 3c**, yellow arrows)⁵, it seems highly likely that the *spam* R1-R8
206 photoreceptors inside the ommatidia would also rotate in an eye-position-dependent manner, resulting
207 in the ventral-dorsal hemispheric DPP mirroring. However, we could not directly confirm this from the
208 round and oval *spam* DPP images (**Fig. 3e**). Nevertheless, in both phenotypes, the photoreceptors'
209 *photomechanical* active sampling makes their receptive fields scan the world in their eye-location-
210 specific directions, broadly matching the flies' concentrically expanding optic flow field during the
211 forward locomotion⁵ (**Supplementary Video 6**).

212

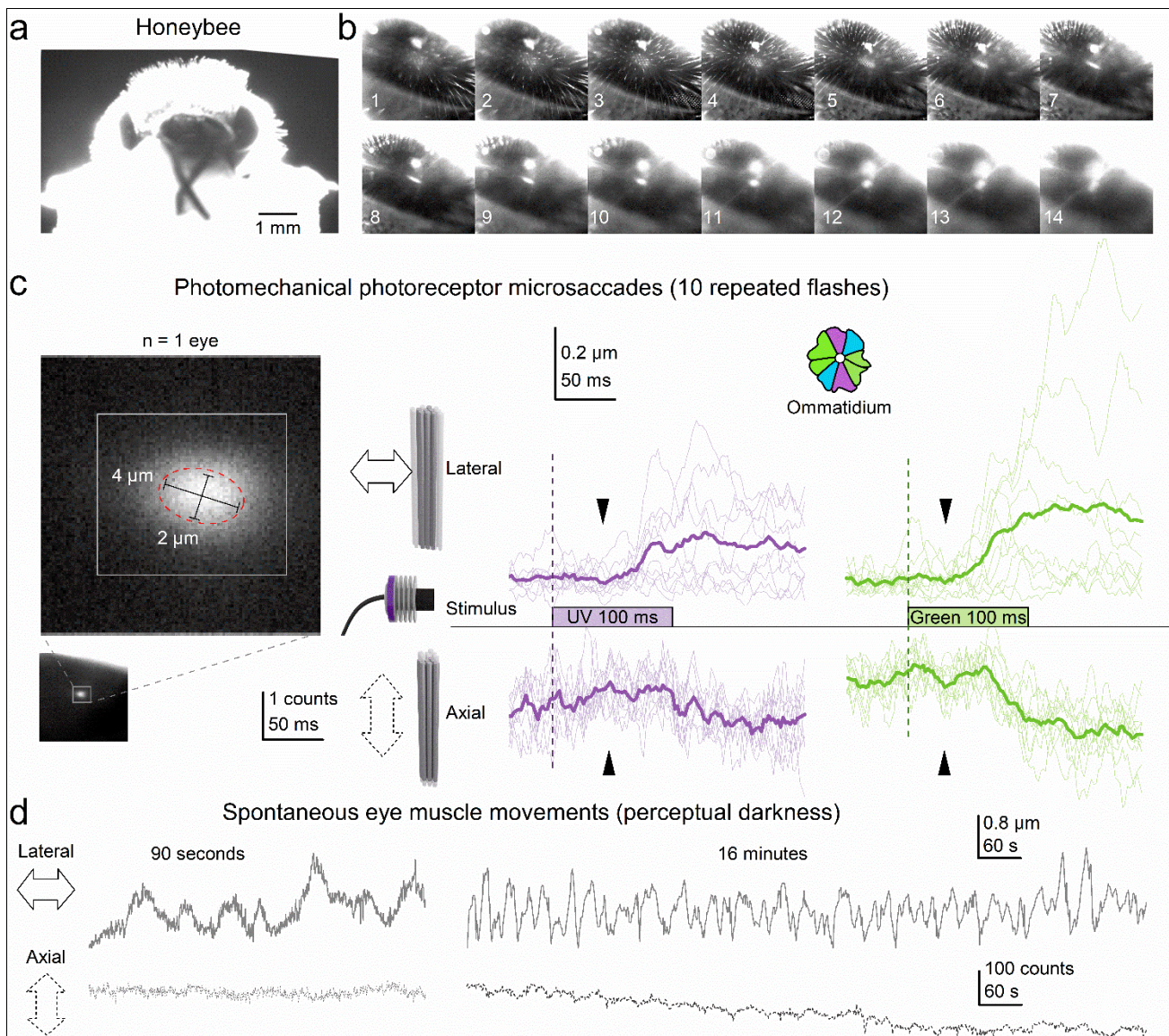


Fig. 7 | DPP microsaccades in honeybee fused rhabdom apposition eyes.

a, Head-immobilised living honeybee prepared for the high-speed DPP imaging experiments.

b, Honeybee compound eye image series under antidromic infrared illumination, when the microscope gradually focusses inside the eye. First, the facet lenses appear (frames #3 and #4) before the DPP emerges as a small bright disk (frames #11 and #12).

c, High-speed imaging of photomechanical photoreceptor microsaccades. A characteristic slightly elongated DPP image of superimposed rhabdoms of neighbouring ommatidia. The DPP elongation is caused by the "ellipsoid" (non-spherical) honeybee eye shape. The scale bars give the actual

rhabdom dimensions in ommatidia. The tested UV and green flashes evoked photomechanical photoreceptor microsaccades, seen as ultrafast lateral DPP "jump" and axial DPP darkening synchronised in time. The average DPP microsaccade to the green flash (green traces) was 1.54-times larger than to the UV flash (purple traces), consistent with the ommatidia having more 1.6-times more green photoreceptors (4) than UV (2.5) photoreceptors (inset).

d, Spontaneous slow eye-muscle-movement-induced (whole retina) DPP drifts were 10-to-100-times slower than light flash triggered photomechanical photoreceptor microsaccades. However, unlike in *Drosophila*⁵, the sluggish eye-muscle-activity shifted the Honeybee DPP positions over seconds and minutes more than the ultrafast (<200 ms) DPP microsaccade displacements superimposed on them.

213

214 **Photoreceptor microsaccades in honeybee fused rhabdom apposition eyes**

215 Our current results, together with those from the previous studies^{4, 5, 8, 9}, indicate that photomechanical
216 transduction reactions within *Drosophila* photoreceptors are responsible for their ultrafast light-
217 induced microsaccades. As these PIP₂-bound reaction steps⁸ are thought to be evolutionarily
218 conserved in rhabdomeric photoreceptors^{32, 33}, we next tested whether the Honeybee (**Fig. 7**) fused
219 rhabdom apposition eyes also generate photomechanical photoreceptor microsaccades.

220

221 The honeybee eyes and head are about 10-times larger than *Drosophila*'s and more densely
222 pigmented, thicker, and sturdier. With long hairs, mouthparts and antennae sticking out, the bee head
223 looks striking, like a 16th-century knight's helmet (**Fig. 7a**). Unfortunately, these structural features
224 complicate GHS-DPP microscopy. The head's thick pigmented cuticle filters out infrared light and the
225 antidromic light path (from the back of the head to the rhabdomere tips) is ~10-times longer than in
226 *Drosophila*. Therefore, we had to surgically remove parts of the rear head cuticle and use a more
227 powerful and condensed infrared beam to achieve sufficiently-high signal-to-noise ratio DPP images
228 of the back-illuminated rhabdoms (**Fig. 7b**). Once a honeybee was aligned correctly, a point-like DPP
229 image of one superimposed rhabdom (**Fig. 7b**, frame #12), collected from the neighbouring

230 ommatidia, emerged with the microscope focussing through the ommatidial surface into the eye.
231 These DPP patterns matched our CG-model prediction (cf. **Fig. 3**) and appeared similar to those in
232 the *spam* fused rhabdom eye (cf. **Fig. 4e**).

233

234 We learned through trial and error not to strive for the best spatial resolution in high-speed imaging
235 experiments. Instead, we optimised the setup to enable high-speed *in vivo* imaging by balancing the
236 infrared power and exposure time with the DPP image contrast and temporal resolution (**Fig. 7c**, left).
237 This optimization process was complex as the temporal resolution was essential to avoid blurring
238 caused by the photoreceptor contractions. Too low infrared power or frame rate, and the small and
239 fast photoreceptor microsaccades were undetectable from the noisy DPP images. Too high power,
240 and the honeybee was near-instantly killed by the heat cooking its brain. However, with appropriate
241 settings, we could repeatedly record bee photoreceptor microsaccades *in vivo* (**Fig. 7c**).

242

243 Honeybee fused rhabdom photoreceptors generated photomechanical microsaccades to both tested
244 UV (**Fig. 7c**, middle) and green light flashes (right); the given examples were recorded after prolonged
245 dark-adaptation. Unsurprisingly, the DPP microsaccades were relatively small, with their maximum
246 displacement range ($\leq 1 \mu\text{m}$) equating to $\leq 1^\circ$ receptive field jumps in space, being close to our earlier
247 prediction⁵. This prediction was based on the bee rhabdom's envisaged "rod-like" rigidity, $\sim 1.9^\circ$
248 receptive field half-width³⁴ and the $\sim 1^\circ$ interommatidial angle¹ (see Discussion). Notably, the green
249 flash evoked on average 1.54-times larger microsaccades than the UV flash. The greater green-
250 sensitivity is consistent with each honeybee ommatidium (**Fig. 7c**, inset) having 4 large green-
251 sensitive photoreceptors and 2.5 UV-sensitive ones (2 large photoreceptors at the opposite walls of
252 each ommatidium + 1 small photoreceptor underneath at the base). In *Drosophila*, the number of light-
253 activated photoreceptors and their combined contraction strength set the DPP microsaccade
254 amplitude⁵. Thus, it seems probable that similar additive photomechanics would govern the Honeybee
255 DPP microsaccades too. Also expectedly, the microsaccades showed synchronised lateral and axial
256 components, comparable to *Drosophila* (**Fig. 5d-l**).

257

258 Nevertheless, whilst indicative of their phototransduction origin, these recorded dynamics were
259 somewhat slower than expected⁵, with the photomechanical rhabdom movements reaching their
260 maxima in about 80-150 ms (**Fig. 7c**), akin to *Drosophila* (**Fig. 5**). The probable explanation for this
261 speed range is the prolonged dark-adaptation, short 100 ms flashes (note, *Drosophila* was tested with
262 200 ms flashes, **Fig. 5a**) and 10 s inter-flash-intervals used in these experiments. After all, dark-
263 adaption is well-known to decelerate honeybee phototransduction dramatically. Interestingly,
264 however, the DPP microsaccades showed a consistent photomechanical transient (a nudge) ~30-50
265 ms from the light onset (black arrows). Such a nudge could, for example, signal a fast and large axial
266 (inward) component, which DPP imaging with suboptimal resolution (of a relatively low signal-to-noise
267 ratio) cannot resolve. Moreover, the microsaccade dynamics varied greatly from trial to trial, even
268 more so than in *Drosophila* (cf. **Fig. 5k**), suggesting that they could be modulated or influenced by
269 intrinsic processes, such as intraocular muscles extruding a force on the ommatidial structures.

270

271 To test whether the photoreceptor microsaccade variability (**Fig. 7c**) could, in part, reflect spontaneous
272 intraocular muscle activity drifting the entire retina (and thus potentially inflicting variable tension to
273 the rhabdoms⁵), we next monitored honeybee DPP continuously in darkness (**Fig. 7d**). These long-
274 term recordings lasted up to 16 minutes. The recordings showed slow wave-like lateral retina
275 movements, occurring about 2-3-times in a minute, and gradual axial creep, almost certainly⁵ pulling
276 the observed rhabdoms inwards (DPP darkening). These spontaneous, presumably muscle-activity-
277 induced, components (**Fig. 7d**) differed clearly from the ultrafast photomechanical photoreceptor
278 microsaccades (**Fig. 7c**). They were largely unsynchronised in time, and most crucially, showed 10-
279 100-times slower dynamics, broadly comparable to our earlier findings of intraocular muscle activity
280 in *Drosophila*^{4, 5}.

281

282 **Discussion**

283 We recorded photoreceptor microsaccades across the wild-type *Drosophila*, *spam* mutant and
284 honeybee compound eyes using a novel infrared GHS-DPP microscopy and analysed their active
285 sampling kinematics. Remarkably, we found the *spam* mutants and honeybee generating ultrafast
286 light-induced microsaccades akin to the wild-type *Drosophila*. Furthermore, in *spam*, the lateral
287 microsaccade movements oriented locally, forming mirror-symmetric left and right eye sampling maps,
288 largely similar to the wild-type flies. These results demonstrate that photoreceptor microsaccades are
289 not limited to the open rhabdom eye design but also occur in fused rhabdom eyes. Most insects,
290 including honeybees, possess fused rhabdom eyes^{23, 24}, in which phototransduction reagents,
291 including PIP₂, are thought to function alike in *Drosophila*^{32, 35}. Therefore, it seems probable that all
292 insect compound eye photoreceptors would generate active sampling.

293

294 **Photomechanical photoreceptor microsaccade dynamics**

295 Photomechanical photoreceptor microsaccades are not reflex-like uniform contractions^{4, 5}. Instead, at
296 each moment, they actively and continuously auto-regulate photon sampling dynamics by moving and
297 narrowing the photoreceptors' receptive fields in respect to environmental light contrast changes to
298 maximise information capture⁴. These dynamics rapidly adapt to immediate light history and are
299 different at dim and bright conditions and to positive (light increments) and negative contrasts (light
300 decrements)^{4, 5}. So, from the viewpoint of sampling theory, photoreceptor microsaccades are not
301 passive but constitute a form of ultrafast *morphodynamic* active sampling^{4, 5}. However, in this study,
302 we only examined photoreceptor microsaccades in one stimulus condition; to bright light flashes after
303 prolonged dark adaptation.

304

305 The *spam* and honeybee DPP microsaccade displacements were generally smaller than the wild-type
306 *Drosophila*'s. This finding is consistent with the inter-rhabdomeric coupling hypothesis⁵. The fused
307 rhabdom rhabdomeres embrace each other and rigidify, and therefore, during microsaccades, they
308 would have less flexibility to move sideways than the open wild-type *Drosophila* rhabdomeres.
309 Conversely, in the much larger honeybee eye, the rhabdoms are further away from the ommatidium

310 lenses, reducing their receptive field sizes and interommatidial angles^{5, 36}. The photoreceptor
311 microsaccades then seem scaled down in proportion to the interommatidial angle, presumably for
312 scanning the best image resolution (**Fig. 8**). These active sampling (or micro-scanning) strategies are
313 not mutually exclusive. Both structure-function relationships could be evolutionarily tuned to scale the
314 insect photoreceptors' active sampling dynamics to each species' unique visual needs. For example,
315 we would predict for fast-flying flies, such as houseflies (*Musca domestica*) and blowflies (*Calliphora*
316 *vicina*), having more ommatidia tiling their eyes more densely, that their photoreceptor microsaccades
317 be smaller and faster than those of slow-flying *Drosophila* of fewer less-densely-packed ommatidia.
318 This way, a fast-eye's photoreceptor receptive fields would sample the world in higher velocity and
319 resolution for higher visual information capture³⁷ - but these high-rate processes would make them
320 metabolically more expensive³⁷ - than those of a slow-eye. The fast eyes should also have more
321 frontal ommatidia with the fastest microsaccades to accentuate acuity⁴ and stereoscopic range⁵ than
322 the slow-eyes.

323

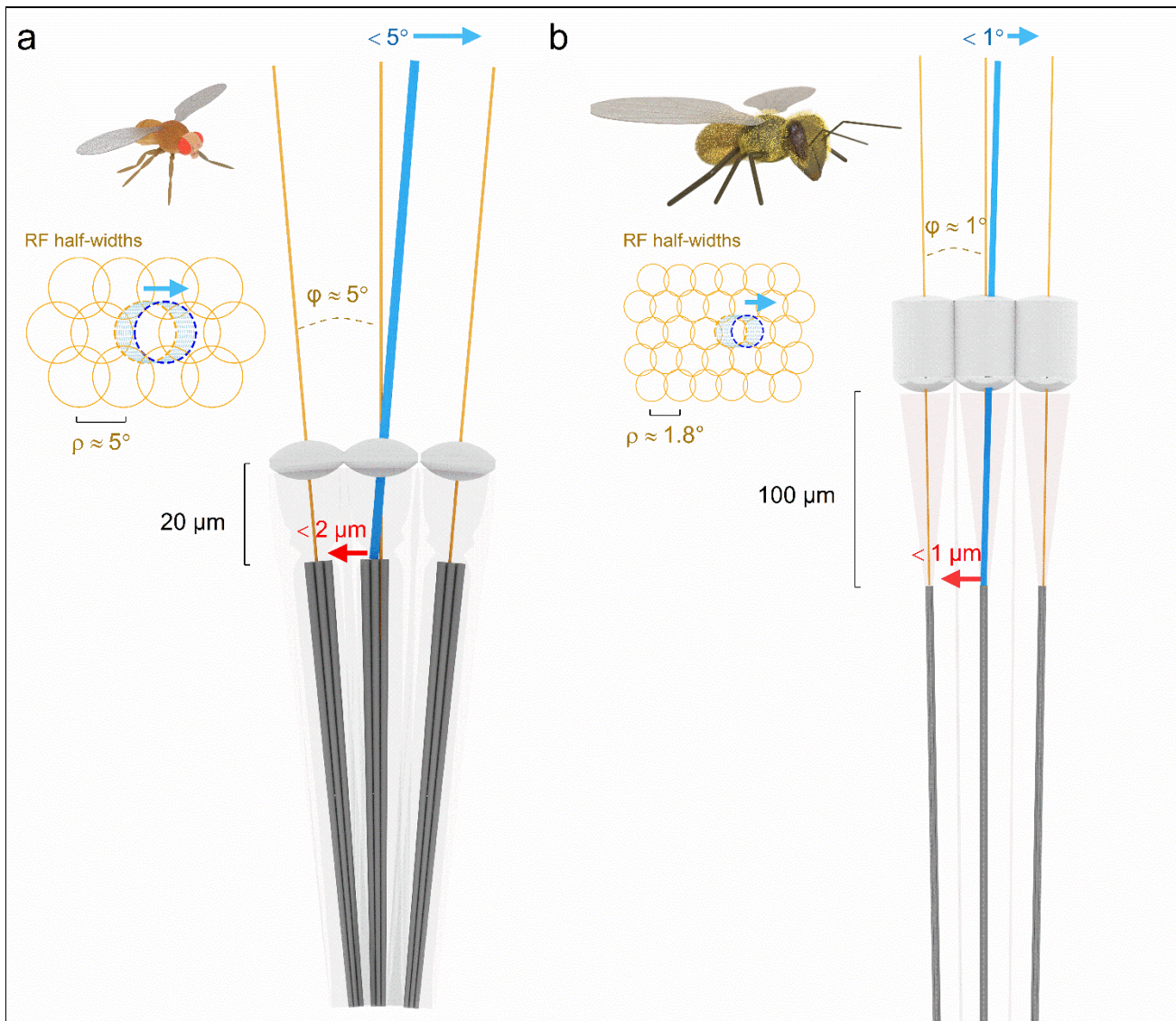


Fig. 8 | Fruit fly and Honeybee photoreceptor microsaccades scale with their receptive field half-width and interommatidial angle, presumably maximising retinal image acuity.

a, *Drosophila* photomechanical photoreceptor microsaccades typically shift their rhabdomeres 1-1.5 µm laterally (max <math>< 2 \mu\text{m}</math>), equating to $\sim 3\text{-}4.5^\circ$ receptive field movements in the visual space. R1-R6 photoreceptors' receptive field half-widths ($\Delta\rho$, retinal pixels) are between $4.5\text{-}6^\circ$, over-completely tiling up the visual space^{4, 5}. The average interommatidial angle³⁸ (ϕ) is $4.5\text{-}5^\circ$. Now consider this as image sampling by a digital camera. The spatial image information doubles when its sensor is moved, and two consecutive images are taken a 1/2-pixel apart and time-integrated for enhanced resolution. But if a pixel (receptive field) moves more, it eventually fuses with its

neighbour (if that neighbour pixel was still – i.e. not detecting light changes). Because of this complete pixel fusion, acuity would decrease as the resulting neural image would contain fewer pixels. Therefore, by limiting micro-scanning to interommatidial angle, *Drosophila* can time-integrate a neural image, which greatly surpasses its compound eyes' optical limits^{4, 5}.

b, Honeybee photoreceptor microsaccades shift their receptive field maximally $<1^\circ$, approaching the eye's average interommatidial angle¹. Equally, such displacement is less than their average receptive field half-width ($\sim 1.8^\circ$) in the front of the eye³⁴. As this active sampling strategy is broadly comparable to that of *Drosophila*, we predict that honeybee vision surpasses its compound eyes' static pixelation limit, similar to what we have shown for *Drosophila*^{4, 5}.

324

325 Ultrafast microsaccades of dissociated *ex vivo* *Drosophila* photoreceptors show both *lateral* and *axial*
326 components⁴, implying that underneath the ommatidial lenses, light changes make photoreceptors
327 bounce inwards and outwards and sideways in a complex piston motion^{4, 5}. GHS-DPP microscopy
328 can reveal both of these components (**Fig. 5d** and **7c**), enabling us to estimate how they shape the
329 way photoreceptors encode visual space in neural time through modelling^{4, 5}. The axial component
330 pulls the rhabdomere away from the ommatidium lens to collect light from a narrower angle. The lateral
331 component makes the resulting receptive field scan the visual space. GHS-DPP microscopy produces
332 2D image sequences ideal for measuring the *lateral* photoreceptor microsaccade dynamics. However,
333 the method detects less well their *axial* components, moving rhabdomeres to and from the ommatidial
334 lens. The estimation becomes less reliable the further away the rhabdom/rhabdomeres are from the
335 ommatidium lens. Following the laws of physics, the proportional DPP intensity change
336 (brightening/darkening), indicating the axial rhabdomere movement, diminishes with distance⁵.
337 Therefore, GHS-DPP imaging can underestimate the overall microsaccade dynamics if these show
338 little sideways movement but have a larger (concealed) axial component. We suspect this would be
339 the case with the honeybee photoreceptor microsaccades. Honeybee rhabdoms are 4.5-times longer
340 than *Drosophila* rhabdomeres, thus having greater potential for axial contraction, but positioned about
341 100 μm from the ommatidium lens³⁹; 5-times the distance in *Drosophila*³⁶.

342

343 **Photoreceptor microsaccade movement direction maps**

344 The microsaccades in the *spam* mutants were slightly more rotated than the wild-type. Nevertheless,
345 with such minor differences, their global maps should broadly match the forward flight optic flow field,
346 similar to what we have previously shown for the wild-type⁵. Theoretically, this correspondence
347 between active sampling and optic flow should improve the visual resolution of the moving world⁵. We
348 further conjectured that since the microsaccades follow the R1-R2-R3 rhabdomere orientation axis⁵
349 (**Supplementary Video 5**), their movement directions are set during development, perhaps guided by
350 some lowest resistance (minimum energy) anchoring⁵. Thus, the observed wild-type and *spam*
351 microsaccade direction differences could reflect slight differences in their R1-R7/8 rhabdomere
352 orientations. Unfortunately, in the circular-symmetric *spam* DPP, the separate R1-R7/8 rhabdomeres
353 are not directly identifiable under infrared illumination. In the future, this hypothesis could be tested by
354 expressing GFP in selected R1-R7/8 photoreceptors or rhabdomeres. Moreover, because the high-
355 speed imaging in the larger and densely pigmented honeybee eyes was experimentally challenging,
356 we also left mapping their microsaccade movement directions for future studies.

357

358 **Photoreceptor microsaccades and eye-muscle-induced whole retina movements mix**

359 Some sporadic interference in the measured microsaccades can originate from the intraocular
360 muscles' activity, which exerts force on the retina. But since such muscle activity typically occurs over
361 much longer time intervals²¹ or during active viewing⁶, being practically absent in firmly restrained
362 flies⁵ and sluggish in head-immobilised honeybees, the eye muscle induced movements had little
363 influence on the ultrafast photomechanical microsaccades shown in this report (i.e. influencing them
364 perhaps only through variable ommatidial tension).

365

366 However, during normal behaviours (in non-restricted, free-moving conditions), the local
367 photoreceptor microsaccades and the global eye-muscle-induced whole retina movements must
368 interact in active sampling. On the top of any eye-muscle-induced whole retina movements, the

369 photomechanical photoreceptor microsaccades will ensue, leading to complex superimposed
370 spatiotemporal ("super-saccadic") sampling dynamics. This sophistication arises because each retina
371 movement will change its photoreceptors' light input, evoking their photomechanical microsaccades.
372 Notably, active sampling can be even more elaborate if the eye-muscle-induced whole retina
373 movements were partly voluntary and depended upon the attentive state. In those circumstances, an
374 insect could use eye-muscle-induced retina movements together with other directional senses, such
375 as antennal casting⁴⁰, to get a better idea of what an encountered object might be. After all, integration
376 of multisensory information reduces uncertainty, increasing fitness.

377

378 Finally, we note that there are uncontrolled genetic differences between the wild-type and *spam*
379 phenotypes, which could potentially contribute to their observed DPP microsaccade differences.
380 Nevertheless, such differences would not alter the general demonstration of the active sampling of
381 the fused rhabdom eye photoreceptors as it occurs with somewhat comparable dynamics to the
382 honeybee rhabdom.

383

384 **Conclusions**

385 Goniometric high-speed deep pseudopupil (GHS-DPP) microscopy provides an innovative non-
386 invasive way to image photoreceptor microsaccades globally across the left and right eyes, or locally,
387 in great detail at specific eye locations. We explained how to use it and gave out free open-source
388 (GPLv3) software tools to quantify and compare active sampling in different insect eyes. Our results
389 demonstrate active sampling both in open and fused rhabdom eyes. Thus, the GHS-DPP microscopy
390 shows real potential as a powerful tool to study how the insect eyes actively sample the visual world.

391

392 Authors declare no competing interests.

393

394 **Author Contributions**

395 Conceptualization (MJ, JK, JT), Data curation (JK, NM), Formal Analysis (JK), Funding acquisition
396 (MJ), Investigation (JK, NM, JT, MJ), Methodology (JK, JT, MJ), Project administration (MJ),
397 Resources (MJ), Software (JK, JT), Supervision (MJ), Validation (JK, JT, MJ), Visualization (JK, MJ),
398 Writing – main paper original draft (JK), Writing – review & editing (MJ, JK, JT).

399

400 **Funding**

401 This work was supported by Jane and Aatos Erkkö Foundation Fellowships (MJ and JT), The
402 Leverhulme Trust (RPG-2012–567: MJ), the BBSRC (BB/F012071/1, BB/D001900/1 and
403 BB/H013849/1: MJ), the EPSRC (EP/P006094/1: MJ), the Open Research Fund of the State Key
404 Laboratory of Cognitive Neuroscience and Learning (MJ), High-End Foreign Expert Grant by Chinese
405 Government (GDT20151100004: MJ).

406

407 **Acknowledgements**

408 We kindly thank Andrew Zelhof for the spam fly line and Gonzalo de Polavieja, Roger C Hardie, Merlin
409 Juusola, Gregor Belušič and the Juusola laboratory members for discussions and comments.

410

411 **1 Data Availability Statement**

412 The software code and datasets for this study can be found in the [https://github.com/JuusolaLab/GHS-](https://github.com/JuusolaLab/GHS-DPP_paper)
413 [DPP_paper](https://github.com/JuusolaLab/GHS-DPP_paper)

414

- 415 1. Land, M.F. Visual acuity in insects. *Annu Rev Entomol* **42**, 147-177 (1997).
- 416 2. Laughlin, S.B. The role of sensory adaptation in the retina. *J Exp Biol* **146**, 39-62 (1989).
- 417 3. Barlow, H.B. The size of ommatidia in apposition eyes. *J Exp Biol* **29**, 667-674 (1952).
- 418 4. Juusola, M. et al. Microsaccadic sampling of moving image information provides *Drosophila*
419 hyperacute vision. *Elife* **6** (2017).
- 420 5. Kemppainen, J. et al. Binocular Mirror-Symmetric Microsaccadic Sampling Enables *Drosophila*
421 Hyperacute 3D-Vision. *bioRxiv* (2021).
- 422 6. Franceschini, N., Chagneux, R., Kirschfeld, K. & Mucke, A. in *Gottingen Neurobiology Report: Synapse*
423 *- Transmission Modulation*. (eds. N. Elsner & H. Penzlin) 1 (Georg Thieme Verlag, Stuttgart, New
424 York; 1991).

- 425 7. Hengstenberg, R. Eye muscle system of housefly *Musca-Domestica* .1. Analysis of clock spikes and
426 their source. *Kybernetik* **9**, 56-77 (1971).
- 427 8. Hardie, R.C. & Franze, K. Photomechanical responses in *Drosophila* photoreceptors. *Science* **338**, 260-
428 263 (2012).
- 429 9. Hardie, R.C. & Juusola, M. Phototransduction in *Drosophila*. *Curr Opin Neurobiol* **34**, 37-45 (2015).
- 430 10. Franceschini, N. & Kirschfeld, K. Optical study *in vivo* of photoreceptor elements in compound eye of
431 *Drosophila*. *Kybernetik* **8**, 1-13 (1971).
- 432 11. Franceschini, N. & Kirschfeld, K. Phenomena of pseudopupil in compound eye of *Drosophila*.
433 *Kybernetik* **9**, 159-182 (1971).
- 434 12. Franceschini, N. in Information processing in the visual systems of *Anthropods* (ed. R. Wehner) 75-82
435 (Springer-Verlag, Berlin, Heidelberg, New York; 1972).
- 436 13. Douglass, J.K. & Wehling, M.F. Rapid mapping of compound eye visual sampling parameters with
437 FACETS, a highly automated wide-field goniometer. *J Comp Physiol A* **202**, 839-851 (2016).
- 438 14. Muñoz Arias, M., Douglass, J.K., Wehling, M.F. & Stavenga, D.G. Automated charting of the visual
439 space of insect compound eyes. *arxiv* (2021).
- 440 15. Kurada, P. & O'Tousa, J.E. Retinal degeneration caused by dominant rhodopsin mutations in
441 *Drosophila*. *Neuron* **14**, 571-579 (1995).
- 442 16. Zelhof, A.C., Koundakjian, E., Scully, A.L., Hardy, R.W. & Pounds, L. Mutation of the photoreceptor
443 specific homeodomain gene Pph13 results in defects in phototransduction and rhabdomere
444 morphogenesis. *Development* **130**, 4383-4392 (2003).
- 445 17. Huang, Y., Xie, J. & Wang, T. A fluorescence-based genetic screen to study retinal degeneration in
446 *Drosophila*. *Plos One* **10**, e0144925 (2015).
- 447 18. Seidl, R. & Kaiser, W. Visual field size, binocular domain and the ommatidial array of the compound
448 eyes in worker honey bees. *J Comp Physiol A* **143**, 17-26 (1981).
- 449 19. Taylor, G.J. et al. Bumblebee visual allometry results in locally improved resolution and globally
450 improved sensitivity. *Elife* **8**, e40613 (2019).
- 451 20. Aptekar, J.W. et al. Method and software for using m-sequences to characterize parallel components
452 of higher-order visual tracking behavior in *Drosophila*. *Front Neural Circuits* **8**, 130 (2014).
- 453 21. Hengstenberg, R. in Information Processing in the Visual Systems of Anthropods 93-96 (Springer,
454 1972).
- 455 22. Wardill, T.J. et al. Multiple spectral inputs improve motion discrimination in the *Drosophila* visual
456 system. *Science* **336**, 925-931 (2012).
- 457 23. Zelhof, A.C., Hardy, R.W., Becker, A. & Zuker, C.S. Transforming the architecture of compound eyes.
458 *Nature* **443**, 696-699 (2006).
- 459 24. Osorio, D. Spam and the evolution of the fly's eye. *Bioessays* **29**, 111-115 (2007).
- 460 25. Ready, D.F., Hanson, T.E. & Benzer, S. Development of the *Drosophila* retina, a neurocrystalline
461 lattice. *Dev Biol* **53**, 217-240 (1976).
- 462 26. Hardie, R.C. in Progress in Sensory Physiology. (eds. H. Autrum et al.) (Springer, Berlin; 1985).
- 463 27. Tang, S. & Juusola, M. Intrinsic activity in the fly brain gates visual information during behavioral
464 choices. *Plos One* **5** (2010).

- 465 28. Zheng, L. et al. Feedback network controls photoreceptor output at the layer of first visual synapses
466 in *Drosophila*. *J Gen Physiol* **127**, 495-510 (2006).
- 467 29. van Swinderen, B. Attention-like processes in *Drosophila* require short-term memory genes. *Science*
468 **315**, 1590-1593 (2007).
- 469 30. Fujiwara, T., Cruz, T.L., Bohoslav, J.P. & Chiappe, M.E. A faithful internal representation of walking
470 movements in the *Drosophila* visual system. *Nat Neurosci* **20**, 72-81 (2017).
- 471 31. Juusola, M. & Song, Z. How a fly photoreceptor samples light information in time. *J Physiol-London*
472 **595**, 5427-5437 (2017).
- 473 32. Fain, G.L., Hardie, R. & Laughlin, S.B. Phototransduction and the evolution of photoreceptors. *Curr*
474 *Biol* **20**, R114-124 (2010).
- 475 33. Juusola, M., Song, Z. & Hardie, R.C. in Encyclopedia of Computational Neuroscience. (eds. D. Jaeger &
476 R. Jung) 2359-2376 (Springer New York, New York, NY; 2015).
- 477 34. Rigosi, E., Wiederman, S.D. & O'Carroll, D.C. Visual acuity of the honey bee retina and the limits for
478 feature detection. *Sci Rep-Uk* **7** (2017).
- 479 35. Yau, K.W. & Hardie, R.C. Phototransduction motifs and variations. *Cell* **139**, 246-264 (2009).
- 480 36. Stavenga, D.G. Angular and spectral sensitivity of fly photoreceptors. II. Dependence on facet lens F-
481 number and rhabdomere type in *Drosophila*. *J Comp Physiol A* **189**, 189-202 (2003).
- 482 37. Song, Z. & Juusola, M. Refractory sampling links efficiency and costs of sensory encoding to stimulus
483 statistics. *J Neurosci* **34**, 7216-7237 (2014).
- 484 38. Gonzalez-Bellido, P.T., Wardill, T.J. & Juusola, M. Compound eyes and retinal information processing
485 in miniature *dipteran* species match their specific ecological demands. *P Natl Acad Sci USA* **108**,
486 4224-4229 (2011).
- 487 39. Varela, F.G. & Wiitanen, W. The optics of the compound eye of the honeybee (*Apis mellifera*). *J Gen*
488 *Physiol* **55**, 336-358 (1970).
- 489 40. Baker, K.L. et al. Algorithms for Olfactory Search across Species. *J Neurosci* **38**, 9383-9389 (2018).
- 490 41. Juusola, M., Dau, A., Zheng, L. & Rien, D.N. Electrophysiological method for recording intracellular
491 voltage responses of *Drosophila* photoreceptors and interneurons to light stimuli *in vivo*. *Jove-J Vis*
492 *Exp* (2016).
- 493 42. Juusola, M. & Hardie, R.C. Light adaptation in *Drosophila* photoreceptors: I. Response dynamics and
494 signaling efficiency at 25 degrees C. *J Gen Physiol* **117**, 3-25 (2001).
- 495 43. Bradski, G. & Kaehler, A. OpenCV. *Dr. Dobb's J Software Tools* **3** (2000).
- 496 44. Virtanen, P. et al. SciPy 1.0: fundamental algorithms for scientific computing in Python. *Nat Methods*
497 **17**, 261-272 (2020).

498

499 **Methods**

500 We describe the GHS-DPP imaging system hardware configuration, how to prepare the flies,
501 experimental protocols, and data analysis tools and principles. All software - from recording to analysis
502 - are available under a free and open (GPLv3) software license in a GitHub repository:

503 https://github.com/JuusolaLab/GHS-DPP_paper.

504

505 **Supplementary Videos 1-2** show how the GHS-DPP microscopy was put together and works.

506 **Supplementary Video 3** shows how ommatidial rhabdomere orientation across the *Drosophila* eyes
507 matches the optic flow field during forward translation.

508 **Supplementary Video 4** shows the relationship between the number of locally activated
509 photoreceptor microsaccades, the angular size of the light stimulus and the number of ommatidial
510 photoreceptors pooled in the deep pseudopupil imaging (given the microscope system's numerical
511 aperture, NA).

512 **Supplementary Videos 2 and 5** show how active sampling - by photomechanical photoreceptor
513 microsaccades - looks like in slow motion and how the microsaccades were analysed across the
514 compound eyes.

515 **Supplementary Video 6** shows how photoreceptor microsaccade movement directions match the
516 ommatidial rhabdomere orientation across the *Drosophila* eyes.

517

518 **Experimental setup**

519 The GHS-DPP imaging system's two primary components are a rotation stage system and a
520 stereomicroscope (**Fig. 2a**). The rotation system allows precise control over the fly eyes' yaw and
521 pitch using two perpendicularly mounted rotation stages (Thorlabs PR01/M, USA), mounted
522 horizontally and vertically. An additional small 3-axis micromanipulator, connected to the vertical
523 rotation stage, was used to control the fly's initial position. Crucially, the vertical rotation stage further
524 rested on a 2-axis micromanipulator so that the intersection point of the two rotation stage axes could
525 be centred at the microscope's field of view. The rotation stage positions were acquired digitally, using
526 two 1024-step rotation encoders (YUMO E6B2-CW23E) and an Arduino board (Arduino Uno, Italy)
527 running a custom C++ program (**Fig. 2b**). In addition, the rotation stages were fitted with stepper
528 motors for fully automated experiments (**Fig. 2a**). Still, in this study, the experiments were performed
529 manually, accurately focussing on DPP at all tested eye locations. **Supplementary Video 1** shows

530 how the GHS-DPP microscope system was put together. Note that the stereo microscope's horizontal
531 mounting is not critical but resulted from our earlier design choices. By having an upright rotation
532 stage, this configuration works well for the binocular compound eye measurements.

533

534 The stereomicroscope was mounted sideways to function with the rotation stages. A high-intensity
535 ultraviolet LED (UV-OptoLED, Cairn Research, UK) was inserted in the microscope's ocular slot,
536 enabling direct light stimulation of the observed DPP rhabdomeres. This 365 nm UV-LED and the two
537 infrared 850 nm LEDs (IR-OptoLED, Cairn Research, UK), which provided antidromic non-stimulating
538 illumination of the DPP rhabdomeres (without activating their phototransduction) through the fly head
539 capsule, were connected to their separate driver units (Dual OptoLED Power Supply, Cairn Research,
540 UK). The LEDs were controlled over the BNC interface using a computer connected data acquisition
541 system (PCI-6221 with BNC-2090A and PCI-6733 with BNC-100, National Instruments, USA) (**Fig.**
542 **2c**). The two infrared LEDs were mounted apart from each other at different angles to prevent the
543 pipette tip or the fly body from blocking the illumination, which would otherwise frequently happen with
544 a single point source. Both the infrared LEDs were in bespoke holders, having a convex lens with
545 adjustable lens-to-LED distance enabled beam focusing. The second unit mounted to the microscope
546 was the high-speed optical camera (Orca Flash 4.0 C13440, Hamamatsu, Japan), which also sent a
547 trigger signal over the BNC interface to the data acquisition system to time the stimulus delivery
548 precisely. We typically acquired 2,048 x 2,048 pixel full-frame images at 100 fps, and occasionally -
549 by cropping the sensor to 2,000 x 200 pixel - collected images at 1,000 fps. The camera had a
550 transparent infrared and opaque UV filter on its pathway, ideally stopping the UV stimulation light from
551 reaching and polluting the image sensor (**Fig. 2d**). Besides these filters, the microscope was
552 configured with a beam-splitter (SZX-BS, Olympus, Japan), a photo adapter piece (SZ-PHA, Olympus,
553 Japan) and a magnification changer (U-TVAC, Olympus, Japan).

554

555 The setup was mounted on a vibration isolation table (air table), which uncoupled any building
556 vibrations that could affect the motion analysis results. The rotation stage system was connected to

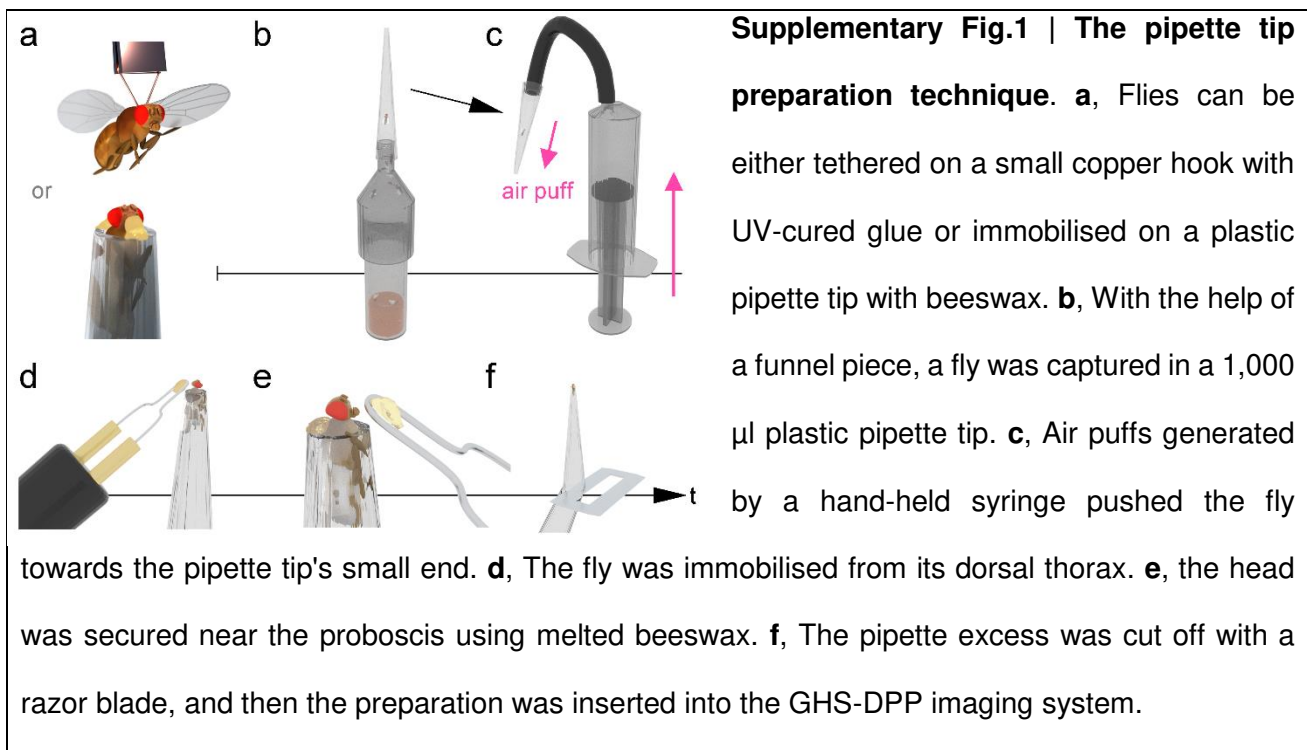
557 the table by magnetic clamps (Magnetic Stand, World Precision Instruments), whilst the microscope
558 system - attached to a thick steel pole of a steel base plate - was heavy enough to ensure its fixed
559 position. The whole setup was enclosed inside a black-painted metal cubicle, with its only open side
560 supporting black curtains for performing the experiments in controlled, dark conditions. Accordingly,
561 the Arduino board's few surface-mounted LEDs were covered with electrical insulation tape to
562 minimise any light noise.

563

564 **Flies and preparation**

565 We used wild-type *Drosophila* flies (Berlin) and a fused rhabdom *spam* null-mutant line (*w*;
566 *spam1/spam1* Frt; sqh-GFP/Tm6B, a gift from Andrew Zelhof) in the experiments. The flies were
567 maintained in an incubator at 25 °C, under a 12:12h light-dark cycle. Only healthy 3- to 20-days-old
568 male and female flies, climbing up the vial, were selected for the experiments. We avoided using very
569 young flies (< 3 days) because their soft heads could bulge during the imaging, presumably due to
570 spontaneous eye muscle activity. The flies were prepared for the experiments using the plastic pipette
571 tip immobilisation technique⁴¹ (**Supplementary Fig.1**). Previously, we tested a copper hook tethering
572 technique⁵, allowing simultaneous behavioural experiments (**Supplementary Fig.1a**). But because
573 both these immobilisations gave broadly similar results⁵, the more laborious and time-consuming
574 tethering was not used here.

575



576

577 In the pipette-tip-fixation method, a 1,000 µl plastic pipette tip was first linked to a funnel piece, and
578 the funnel was connected to a vial full of flies. One fly at a time was lured into the pipette tip through
579 the funnel driven by *Drosophila*'s innate geotaxis behaviour (**Supplementary Fig.1b**). This way, there
580 was no need to immobilise the flies by CO₂ or ice-cooling that could potentially affect the
581 microsaccades. Next, the pipette tip was viewed under a stereo preparation microscope (Olympus
582 SZX-9, Japan). At the same time, the fly was gently pushed towards the tip opening by puffing air from
583 a hand-held syringe (**Supplementary Fig.1c**). When needed, the pipette tip's opening was adjusted
584 using a razor blade to ensure that the fly head passed through without any deformation, minimising
585 structural damage to the eyes. The fly was air-puffed until its head and upper thorax protruded the tip
586 end. When the fly was ideally positioned, it was quickly immobilised by applying melted beeswax on
587 its thorax (**Supplementary Fig.1d**) and ventrally to its head and proboscis (**Supplementary Fig.1e**).
588 In this correct position, the pipette would not shadow the dual-IR illumination during the experiments.

589

590 Additionally, the proboscis could have been pulled out with forceps and waxed on the pipette's outside,
591 or the antennae waxed. However, these manoeuvres, which we often use in preparing *Drosophila* for

592 intracellular electrophysiology^{41, 42}, were omitted because they made no difference in the observed
593 microsaccades. Furthermore, these procedures would have prolonged the preparation making,
594 potentially increasing structural damage. Conversely, some more wax was routinely applied on the
595 dorsal side of the head, under the ocelli, to secure the head position further. Finally, the pipette was
596 cut from its large end using a razor blade (**Supplementary Fig.1f**), and the preparation was carefully
597 placed in the setup (**Supplementary Video 2**).

598

599 **Honeybee**

600 Honeybees (*Apis mellifera*) were kept indoors in a hive that provided the bees an outside
601 (nature) access through a plastic portal. Worker bees were captured from the portal and
602 prepared using the pipette tip technique similar to the *Drosophila* with few adjustments. First, the
603 pipette tip's small opening was cut larger to fit the bee head. Second, the bee was ice-cooled before
604 the waxing to prevent it from escaping. During the cooling, the bee inside a plastic vial was placed in
605 ice until its leg movements temporarily halted. Although the bees quickly recovered, as judged by their
606 antennal movements, the ice-cooling may have generally affected their physiology. Finally, a cuticle
607 section (between the antennae and ocelli and the dorsal part of the eyes) was removed by a razor
608 blade after the waxing. This microsurgery greatly increased the DPP image's brightness, allowing us
609 to image photoreceptor microsaccades in high frame rates (100Hz and 500 Hz).

610

611 **Data acquisition and software**

612 To enable non-specialist users to operate the GHS-DPP microsaccade imaging experiments, we
613 created a free and open (GPLv3) recording software called *Gonio Imsoft*. *Gonio Imsoft* interfaced with
614 the open-source microscopy software *MicroManager* to control the high-speed camera. In addition, it
615 used the *NI-DAQmx* module (controlling the data acquisition) and the *PySerial* module
616 (communicating with the Arduino microcontroller), reading out the rotary encoders. *Gonio Imsoft* ran
617 on a Windows 10 platform.

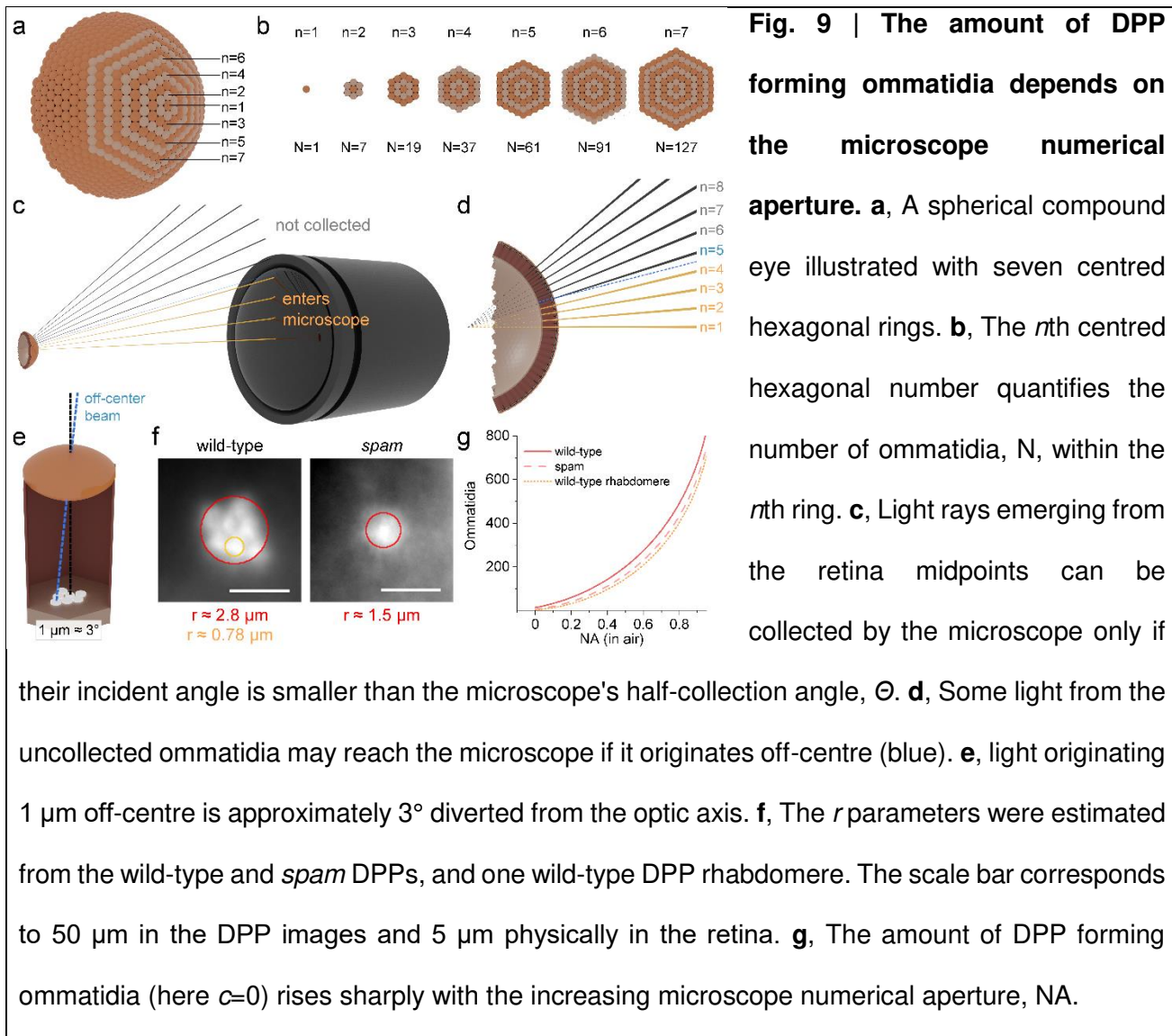
618

619 We used the Olympus DF-PLAPO 1X objective for typical experiments with the microscope's
620 continuous zoom maxed out and the additional magnification changer set to the 2x-position. In this
621 configuration, a small-to-average-size fly head falls entirely within the field of view. The microscope's
622 light path selector was set to its mid-state, resulting in an 80%/20% light intensity split between the
623 camera and the eyepieces, respectively. The two infrared illumination LEDs were focused on the back
624 of the fly head. Using the 2-axis micrometre, mounted on the horizontal rotation stage, the vertical
625 rotation stage was centred so that the fly head, when brought to the field-of-view by the 3-axis
626 micromanipulator (mounted on the vertical rotation stage), remained in the centre of the field of view
627 in all possible horizontal and vertical rotation combinations (**Supplementary Video 2**). However, the
628 microscope's focus remained only approximately correct since the fly head is not perfectly round and
629 hence refocusing was needed to maintain a sharp DPP image during the experiments.

630

631 The microscope was first focused so that the ommatidial lenses appeared crisp and clear. Then, the
632 focus was brought deeper into the eye until the DPP became clear and visible. In this ommatidial axes'
633 converge point, images formed by individual ommatidia superimpose, creating a magnified, virtual
634 image of the rhabdomere tips¹¹ (**Supplementary Video 4**). Using our computer graphics (CG)
635 simulations on wild-type and *spam* eyes, we further confirmed that the retinal patterning (**Fig. 1a** and
636 **b**) indeed resulted in a one-spot DDP image in the *spam* (**Fig. 1c**).

637



638

639 The DPP is purely an optical phenomenon, informing us more about how the observed rhabdomere
 640 summation image is affected by the used microscope system¹¹ than how the fly compound eye
 641 converges visual inputs from the world²⁸. Therefore, the DPP cannot tell us too much about the eyes'
 642 neural superposition design, in which R1-R6 photoreceptor outputs from six neighbouring ommatidia,
 643 sampling light over the same small visual area, are synaptically pooled. Nevertheless, it is helpful to
 644 estimate the number of ommatidia forming in the optical DPP image as this improves our
 645 understanding of any blurring and irregularities in it. On a hexagonal tiling, the number of hexagons
 646 within an n th concentric hexagonal circle (**Fig. 9a** and **b**) can be calculated using the formula

647

648
$$\begin{cases} N = 3n(n - 1) + 1 & \text{if } n \geq 1 \\ N = n & \text{if } n < 1 \\ N = 0 & \text{if } n \leq 0 \end{cases} \quad (1)$$

649

650 The values of N are known as the centred hexagonal numbers. The piecewise formulation also
651 accounts for the $n < 1$ cases, usually left undefined. By finding the right n , we use it to denote the
652 number of ommatidia participating in the DPP image formation. From the eye-microscope geometry
653 (**Fig. 9c** and **d**), we can estimate the value of n , after which the illumination light rays no longer can
654 enter the microscope's entrance pupil, and write

655

656
$$n = \frac{\theta + 2(0.5 - c)\alpha}{\Delta\varphi} + 1 \quad (2)$$

657

658 θ is the half-angle subtended by the microscope lens to the eye, $\Delta\varphi$ is the interommatidial angle, c is
659 the minimum counted contribution term and α is the mean deviation angle between the outermost
660 rhabdomere receptive axes and the ommatidial axis. If we were to estimate the number of ommatidia
661 that project all their rhabdomic light to the microscope, $c = 1$, and conversely, if we were interested
662 in ommatidia casting *any* rhabdomic light to the microscope, $c = 0$. For counting ommatidia with
663 other contributions, the correct c depends on the microscope NA. But for a 50% minimum contribution
664 estimate, we can use the former estimates. Then next, ideally, if the rhabdomeres formed a single
665 point on the ommatidial axis (and the eye was perfectly spherical), α would be zero. And, if the
666 rhabdomeres were organised into a hexagonal shape so that the neighbouring rhabdomeres'
667 receptive fields (RFs) perfectly overlap at infinity, α would nearly equal the interommatidial angle $\Delta\varphi$.

668

669 By replacing the half-angle with the numerical aperture (NA) and considering that in *Drosophila* 1 μm
670 displacement results in a 3° angular change⁵, we can write

671

672
$$n = \frac{\sin^{-1}\left(\frac{NA}{m}\right) + 2(0.5 - c) (3^\circ / \mu\text{m } r)}{\Delta\varphi} + 1 \quad (3)$$

673

674 *NA* is the numerical aperture of the used microscope, *m* is the refractive index of microscope objective
 675 immersion medium ($m = 1$ for air), and *r* is the radius of a circle in the ommatidial retinal plane that
 676 representatively contains all the rhabdomeres. The numerical aperture in our microscope system was
 677 0.11, and the *Drosophila* interommatidial angle is approximately 5° ^{36, 38}. Since the DPP image is a
 678 ~10x magnified image of the rhabdomere tips, the *r* parameters for the wild-type and *spam* can be
 679 estimated directly from the DPP still images as 2.8 μm and 1.5 μm (**Fig. 9f**). Inserting these values in
 680 (3) and then calculating (1), we approximate that in our microscope system, 18 ommatidia would
 681 contribute at least 50% to the deep pseudopupil image formation in the wild-type and 12 ommatidia in
 682 the *spam* eye. For one rhabdomere in the wild-type DPP pattern, we can similarly estimate that its *r*
 683 is 0.78 μm (**Fig. 9f**), suggesting that 10 ommatidia form it. Notice, however, that because of the
 684 structural asymmetries, these ommatidium counts are likely slightly overestimated. For example,
 685 the *Drosophila* ommatidial R1-R6 rhabdomeres are not hexagonally arranged around the lens centre.
 686 Instead, their sizes and distances vary⁴, forming an asymmetric (slanted) trapezoid arrangement (**Fig.**
 687 **3c**), and the eye is not perfectly spherical. Moreover, infrared illumination, by passing through the
 688 ommatidial screening pigments that block non-axial green and UV transmission, could potentially
 689 merge more ommatidia into the DPP image than visible light. Nevertheless, since these upper-bound
 690 estimates vary with the used microscope systems (**Fig. 9g**), we calculated them for a range of air-
 691 objective NAs (**Supplementary Table 1**).

692

693 **Supplementary Table 1.** The estimated number of ommatidia forming the DPP image.

Microscope NA (in air)	N (wild-type ommatidia) ($r = 2.8 \mu\text{m}$)			N (<i>Spam</i> ommatidia) ($r = 1.5 \mu\text{m}$)			One wild-type rhabdomere ($r = 0.78 \mu\text{m}$)		
	contributing at least								
	100%	50%	>0%	100%	50%	0%	100%	50%	>0%

0.001	0	7.3	15	0.11	3.2	6.2	0.54	1.8	3.1
0.01	0	8.0	16	0.21	3.7	7.1	0.65	2.2	3.8
0.05	0	11	23	0.67	6.3	12	1.3	4.4	7.4
0.1	0.47	17	33	1.9	11	20	4.4	9.1	14
0.2	4.1	32	61	11	26	41	17	25	32
0.4	38	90	143	56	84	112	68	83	97
0.6	115	195	274	146	189	231	165	187	209
0.8	268	380	492	314	374	434	341	372	403
0.95	521	671	821	585	665	745	622	663	705

694

695 In this study, we performed two kinds of experiments: *local recordings* at a fixed position on the left
696 and right eye and *global recordings* across the eyes. In the local recordings, we imaged one location
697 on the left eye (+28° horizontal and -37° vertical) and another on the right eye (-28° horizontal and -
698 37° vertical) because, at these locations, the upper infrared LED illuminated the eyes ideally, forming
699 the crispest DPP. The stimulus UV-LED was flashed for 200 ms while simultaneously the high-speed
700 camera acquired images 100 frames per second, yielding 20 image frames per flash. As a standard
701 procedure, this recording process was repeated 25 times to obtain the mean photoreceptor
702 microsaccade estimates and inspect their variability in an individual fly. Between the repeats, we
703 initially used 10 s inter-stimulus-interval (ISI) for both the wild-type and spam flies. But ISI was later
704 shortened ISI to 2 s, as there was no significant reduction in the response amplitude. All images were
705 saved as 16-bit unsigned-integer, grayscale TIFF images.

706

707 The global imaging procedure was similar, but it was performed only once at each location. Instead,
708 after each flash, the fly was rotated in 10° steps from -40° to +50° (limited by the vertical rotation stage,
709 covering the microscope objective or the two illumination LEDs) using the horizontal rotation stage.
710 After completing the horizontal "line scan", the vertical rotation stage was advanced in a 10° step,
711 covering a range from -110° to +110°. By rotating the fly and imaging in between, we scanned

712 approximately 200 distinct locations on the left and right eyes. Overall, it took about 10 s to reorient
713 the fly, refocus at the deep pseudopupil and start the image acquisition protocol again.

714

715 **Data analysis**

716 To quantify the 3-dimensional rhabdomere movement fields, we created a free and open (GPLv3)
717 data analysis software called *Gonio Analysis*. It allows drawing regions of interest (ROIs) around the
718 deep pseudopupil, performing motion analysis, and finally, translating the motion results from the
719 camera image coordinates to the fly's 3D frame-of-reference, using the digitally read rotation stage
720 values. Here, we shortly describe its data analysis principles.

721

722 Rectangular ROIs were drawn by hand for the first frame of each location only by selecting the deep
723 pseudopupil. Next, these pseudopupil images were used as template images for cross-correlation
724 based motion analysis (**Fig. 10a**). We used the computer vision library *OpenCV*⁴³ and its
725 *matchTemplate* routine for the following 2D cross-correlation

726

$$727 \quad R(x, y) = \frac{\sum_{x', y'} (T'(x', y') I'(x+x', y+y'))}{\sum_{x', y'} T'(x', y')^2 \sum_{x', y'} I'(x+x', y+y')^2} \quad (4)$$

$$728 \quad T'(x', y') = T(x', y') - \frac{1}{w*h} * \sum_{x'', y''} T(x'', y'')$$

$$729 \quad I'(x+x', y+y') = I(x+x', y+y') - \frac{1}{(w*h)} * \sum_{x'', y''} I(x+x'', y+y'')$$

730

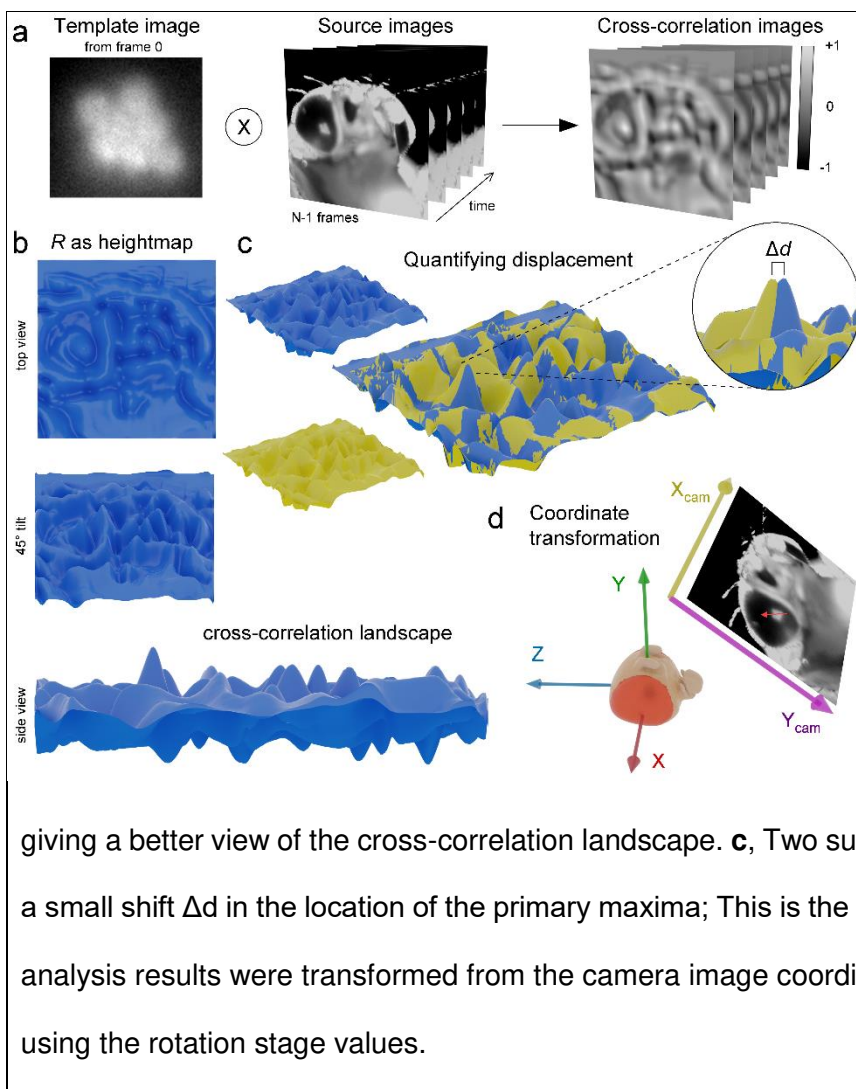


Fig. 10 | Cross-correlation based motion analysis by template matching. **a**, The first frame of the DPP image, manually cropped, was used as the template image. By 2D cross-correlation analysis, the DPP image locations were searched among the source images. **b**, A cross-correlation result image R can be presented as a height-map,

giving a better view of the cross-correlation landscape. **c**, Two superimposed R height-maps reveal a small shift Δd in the location of the primary maxima; This is the DDP displacement. **d**, The motion analysis results were transformed from the camera image coordinates to the fly coordinate system using the rotation stage values.

731

732 R is the 2-dimensional cross-correlation image, and $R(x,y)$ is its value at the pixel (x,y) . x' , x'' and y' , y''
 733 are summation indices within ranges $[0, 1, 2, \dots, w-1]$ and $[0, 1, 2, \dots, h-1]$, w and h are the width and
 734 height of the template image. I is the source image, and T is the template image.

735

736 In the cross-correlation results of the images R produced by the template matching (**Fig. 10b**), the
 737 higher values were signed for the higher similarity between the template and source images at each
 738 location. Therefore, using two source images acquired at different times, the template displacement
 739 between these images can be calculated by comparing their resulting cross-correlation image's peak
 740 values (**Fig. 10c**). Furthermore, we visually confirmed some motion analysis results by creating videos
 741 in which the rectangular ROI box was moved according to the motion analysis results, readily following

742 the moving DPP. On the other hand, we note that computing the complete cross-correlation with
743 uncropped source images (cf. **Fig. 1**) is inefficient and can lead to a false match. Therefore, we instead
744 performed the cross-correlation only in the near vicinity (30 pixels) of the DPP cropping without
745 truncating the responses.

746

747 In the template matching, the motion analysis results were given in the camera image coordinates. To
748 translate them from the camera system to the 3D space in the fly's frame of reference (**Fig. 10d**), we
749 used the digitally read vertical v and horizontal h rotation stage values on the following set of equations

750

$$751 \quad \begin{cases} y = \cos(h) \cos(v) \\ z = y \tan(v) \\ |x| = \sqrt{1 - y^2 - z^2} \end{cases} \quad (7)$$

752

753 to calculate the microscope's (x, y, z) location. Using the same equation set, in short, $P(h, v) \rightarrow (x, y, z)$,
754 we then calculated the camera x unit vector as the vector from $P(h, v)$ to a slightly displaced
755 point $P(h + \Delta h, v)$

756

$$757 \quad \hat{i}_{cam}(h, v) = \overrightarrow{P(h, v) P(h + \Delta h, v)} \quad (8)$$

758

759 where Δh is ideally as small as possible but large enough not to cause errors because of limited
760 floating-point precision. Since the y -camera-unit only depends on the vertical rotation and its x -
761 component in the fly coordinate system is conveniently zero (i.e. the y -unit-vector is always
762 perpendicular to the great circle arc that the microscope travels along from the fly's point of view), it is
763 simply

764

$$765 \quad \hat{j}_{cam}(v) = -\sin(v) \hat{j} + \cos(v) \hat{k} \quad (9)$$

766

767 Finally, the (x, y, z) movement vectors can be then calculated using camera unit vectors as

768

$$769 \quad \mathbf{v}(m_x, m_y, h, v) = m_x \hat{i}_{cam} + m_y \hat{j}_{cam} \quad (10)$$

770

771 where m_x and m_y are the camera image x and y movement values produced by the cross-correlation.

772

773 We averaged the results over many flies using simple N-nearest neighbour interpolation for the

774 microsaccade vector maps acquired in the global recordings. For each interpolation point, from each

775 of the N imaged flies, the nearest 3D vector was selected, but only if the angular distance of the 3D

776 vector was not larger than 2-times the angular interpolation step of 5° . And, these equal or less than

777 N vectors were averaged together only if there were N/2 of them or more. The difference in the wild-

778 type and *spam* vector maps were calculated point-wise as

$$779 \quad e(\mathbf{v}_{wtb}, \mathbf{v}_{spam}) = \frac{1}{\pi} \cos^{-1} \left(\frac{\mathbf{v}_{wtb} \cdot \mathbf{v}_{spam}}{\|\mathbf{v}_{wtb}\| \|\mathbf{v}_{spam}\|} \right) \quad (11)$$

780

781 where \mathbf{v}_{wtb} and \mathbf{v}_{spam} are the microsaccade vectors and the operators \cdot and $\|\cdot\|$ denote the inner

782 product and the vector norm, respectively. Finally, for rotation direction analysis, we rotated the

783 vectors on the x-axis and calculated whether the spam vectors were rotated clockwise or

784 counterclockwise compared to the wild-type and then used this result to sign the error in (11).

785

786 In the local recordings, we focused solely on the directionless microsaccade magnitude, calculated

787 using the Pythagorean theorem from the camera coordinate movement values. From these animal-

788 specific mean magnitude traces, we calculated the microsaccade amplitude, speed, logistic growth

789 factor and half-rise time quantifications. The probability graphs were calculated as 1D-histograms at

790 each time point, with 20 stitched together to cover the whole imaging period. The total displacement

791 values were quantified from the magnitude data by simply taking the mean of the last 7 data points,

792 the last 70 ms of the imaging. The maximum speed was calculated from the highest value between

793 frames displacement. For the logistic growth factor and the half-rise time, we fitted the data with the
794 sigmoidal logistic function

795

$$796 \quad f(t) = \frac{L}{1+e^{-k(t-t_0)}} \quad (12)$$

797

798 where L is the maximum value corresponding to the total rhabdomeric displacement, k is the logistic
799 growth factor that in our case characterises the microsaccade activation phase time-duration, and t_0
800 is the half-rise time.

801

802 **Statistics and Reproducibility**

803 The presented results are readily reproducible. Every healthy *Drosophila* with functional vision will
804 show them. The figures and figure legends give the sample sizes (how many flies were used) and the
805 number of recorded responses (to repeated stimulation). In contrast, because honeybee has black
806 "armoured" head cuticle, which makes preparing them significantly more complicated, we show only
807 exemplary (repeatable and reproducible) results from one bee. These results reveal photoreceptor
808 microsaccades occurring also in the bee eye, with comparable ultra-fast dynamics to *Drosophila*, and
809 demonstrate that GHS-DPP microscopy can capture them too. All the quantified local recording
810 parameters (displacement, speed, growth factor and rise-time) appeared reasonably normally
811 distributed. However, since the *Drosophila* wild-type sample size was 3-times larger than the *spam*
812 one, we used Welch's t-test⁴⁴ that performs better with uneven samples for all comparisons.